Chapter Five

Discussion on Structural and Thermal Properties of Catalysts

This chapter discusses the structural and thermal properties of the best catalysts (*i.e.*, B14 and B11) developed in this work, characterized using the standard analytical procedure as discussed in chapter four. Coincidentally, both catalysts as demonstrated are prepared by DIWI method via citrate-nitrate route (precursor P2); *i.e.*, Cu-Zn at/at ratio 3:1 and Cu-Fe at/at ratio 3:1 respectively.

As stated in the overall research objectives, the characterization data of selected catalysts' lead samples identified from the performance screening programmes discussed in chapter four will be presented here. The selection criteria are based on the highest catalytic performance. As it is crucial to also identify the trend-in each-catalyst series, which is relevant for a rational approach in future catalyst design, some catalysts at a lower catalytic performance are also studied for comparison. Among the selection are the mono-copper catalyst prepared with precursor P2, binary Cu-Fe and also Cu-Zn samples at different at/at ratio (1:3 and 1:1). In order to discriminate also the influence of precursor as supposed to the nitrate route vs. the citrate-nitrate route, another three catalysts were selected, *i.e.*, mono-copper, binary Cu-Fe at/at 3:1 and Cu-Zn at/at 3:1 prepared with P1. The selection of catalysts is listed in Table 5.1.

Table 5.1: Selection of catalysts (supported on silica) for various characterization analysis (highlighted in blues were the superior catalysts in the hydrogenolysis reaction).

Code	Composition	Precursor	Wt Loading	Activity (mmol OH/ g catalyst / hours)
*Sil	Silica CS 2050	-	-	0
B08	Mono-Cu	P2	28.81	37.26
C1	Mono-Zinc	P2	28.25	0.06
B12	Cu-Zn at/at 1:1	P2	28.52	24.21
B13	Cu-Zn at/at 1:3	P2	28.40	26.08
B14	**Cu-Zn at/at 3:1**	**P2**	**28.64**	**78.29**
B01	Mono-Cu	P1	41.00	2.87
B07	Cu-Zn at/at 3:1	P1	29.96	2.93
C2	Mono-Iron	P2	28.25	0.49
B09	Cu-Fe at/at 1:1	P2	22.16	25.16
B10	Cu-Fe at/at 1:3	P2	19.87	33.30
B11	**Cu-Fe at/at 3:1**	**P2**	**25.50**	**50.43**
B04	Cu-Fe at/at 3:1	P1	32.79	8.03

* silica CS2050 as reference (blank)

In this chapter the discussion of characterization results will focus on two series of samples led by catalyst B14 (referred as Cu-Zn series), and by catalyst B11 (referred as Cu-Fe series). A standard reference material containing pure zinc (C1) or iron (C2) supported on silica were also measured for elucidating the effects specific to the presence of copper. That copper is the active element in catalysis becomes evident from inspection of the performance data listed in Table 5.1.

5.1. Structural Analysis

5.1.1. Powder X-ray diffraction (XRD)

The phases and structural integrity of all precursor and calcined samples were inspected using powder X-ray diffraction. Bare silica support which was measured also as reference exhibited a big hump at 15-30° which is a typical characteristic of highly amorphous silica. This prevailing features of silica giving rise to the broad feature is the first maximum of the Si-O pair correlation function.

Generally, all precursor materials prepared via citrate-nitrate route (precursor P2) are X-ray amorphous whereas distinct crystallinity of all samples prepared via the nitrate route (precursor P1) have been observed prior to calcination in air at 723K for 2 hours (Figure 5.1, 5.3, 5.5, 5.7).

Figure 5.1 shows the compilation of XRD pattern for precursor samples of the Cu-Zn series prepared with precursor P2. As mentioned above all samples are X-ray amorphous despite of the metal weight loading of not more than 30wt% (C1, B13, B12, B14 and B08). Samples exhibited very low diffraction intensities, with exception for a single peak that could be clearly observed at the range of 10-12° for the samples C1 and B13. It can be concluded that the 10-12° peak could have been related to the presence/amount of zinc. In Zn rich samples a modification of the stacking of the basic structural units of the support may have resulted in a quasi-periodic superstructure. This would indicate a reaction between Zn and the support that modulates the particle interaction in the aggregate structure of the matrix.

The diffractrogram of precursor material of the Cu-Fe series from those prepared via citrate-nitrate route did not give a lot of information with regards to the possible presence of crystalline phases (Figure 5.5). The strong fluorescence of Fe compounds excited with Cu radiation further reduces the detection limit for small particles of potentially present iron compounds. A little information can be derived only from the precursor sample B11, in which peaks were identified being due to ammonium nitrate with five main peaks at range 15-40° of 2-theta, JCPDS 83-0520. The structure of this compound is orthorhombic.

As mentioned earlier, the precursor samples prepared via the nitrate route already showed good crystallinity before calcination (Figures 5.3 and 5.7). Based on the characterization results from UV-Vis and SEM method, the diffraction peaks were attributed to the large particle sizes compounds from the active elements. This is a negative effect with respect to the performance of materials; as indeed observed in the study of hydogenolysis of methyl laurate. The main peak of 12.87°, 25.90°, 33.78°, 36.68° and 43.80° (2-theta range) in precursor sample B01 and B07 indicates the presence of copper nitrate hydroxide (gerhardite, JCPDS 74-1749) of monoclinic structure. At the same time, twin peaks at 35.65° and 38.73° alongside smaller peaks at 43.83°, 58.07° and 75.21° are due to the presence of CuO (tenorite, JCPDS 45-0937) and partially oxidized Cu_4O_3 (copper oxide, JCPDS 83-1665). The precursor sample B04 also showed similar diffraction pattern which could be linked also to the presence of copper nitrate hydroxide, gerhardite and copper oxide, tenorite. There were no indications of the presence of zinc or iron compounds in precursor sample B07 and B04, respectively.

After calcination, the catalysts consist of amorphous- copper and zinc oxides supported on silica for the Cu-Zn series; and copper and iron oxides supported on silica for the Cu-Fe series. There is no indication of oxidic interaction with supports *e.g.* of the formation of crystalline copper silicates, zinc silicates or iron silicates in all diffractograms. However, in general, the diffractrogram of all materials (calcined and precursor alike) indicate an overall poor crystallinity and do not allow possible detection of phase formation between support and active materials. This is despite of the fact that the composition of the catalysts hardly allows any more to consider them as "impregnated" or supported. The deposited metal precursors and their oxides must be present in highly disordered forms characterizing the materials prepared as metastable with respect to crystallization or ternary phase formation. To which extent these processes have already occurred must be investigated with methods that do not rely on long range crystalline ordering.

The identification of crystalline phases in the calcined material of mono-metallic copper supported on silica, B08 prepared via citrate-nitrate route (Figure 5.2) was easily possible by the presence of twin-peak at 2-theta 35.85° and 38.95° (Table 5.2) which is typical characteristic pattern assigned to tenorite (copper oxide) with monoclinic structure (JCPDS 45-0937, Table 5.4). It can be concluded that the crystalline material of sample B08 has been formed only after the decomposition of metal precursors during the calcination procedure.

In the calcined material of mono-metallic zinc supported on silica, C1 prepared via citrate-nitrate route which is used as standard reference material for all Zn-containing catalyst (Figure 5.2), zinc oxide of hexagonal lattice (JCPDS 36-1451, Table 5.5) with prominent peaks at 2-theta 31.89°, 34.99° and 36.67° is observed. More interestingly

however, is the dissipating of the broad feature of silica in the range of 10-12° which is a clear indication of a strong chemical interaction of zinc with support in the form of zinc silicates.

The XRD pattern of the calcined Cu-Zn material of B12, B13 and B14 prepared via precursor P2 do not show discernible diffraction patterns of crystalline phases (Figure 5.2). This is indicative of the creation of nano-structured supported crystals in all samples prepared via citrate-nitrate route as also observed from the SEM micrographs.

Samples prepared via precursor P1 showed higher crystallinity, in the form of CuO at the same 2-theta position as tabulated in Table 5.2. The catalytic performance of catalyst from the Cu-Zn series suggested that those prepared via citrate-nitrate route gave better activity compared to that prepared via nitrate route. This finding strongly suggests that the nanostructuring of the precursor copper oxide is an important goal in the catalyst preparation procedure.

The most active sample B14 shows the least intense of the CuO twin peak at the same time, apparently exhibited highest likelihood to contain the modified silica by zinc as compared to sample B12 and B13. If such, the XRD pattern of B14 especially suggested the occurrence of nano-particles copper crystal anchored on a zinc-modified silica support, and thus providing highly active material in the hydrogenolysis of ester to alcohol. The best at/at ratio of Cu-Zn at 3:1 suggested that the active working material was copper, and an addition of only a small amount of zinc as textural promoter (to modified support) to the system is necessary (as zinc do not have the right site for the hydrogenolysis reaction) to produce better dispersion of nano-copper particles.

The XRD data of the calcined material of catalysts from the Cu-Fe series (B09, B10 and B11 in Figure 5.6) again clearly show that the catalyst prepared by citrate-nitrate route are nanostructured and show no recognizable diffraction pattern, whereby only in sample prepared via nitrate route *e.g.* B04 in Figure 5.8, reflections of the large crystallites of CuO are discernible as the twin peak superimposed on the pattern from the support. This is in agreement with the SEM micrographs of these samples. No conclusion can be achieved as there is not enough information to be collected with regards to the iron compound supported on silica, C2. Nevertheless, the performed Cu-Fe catalysts (as in the Cu-Zn series) are also observed as those poorly crystalline, tend to exhibited more amorphous-like feature or generally in a state of fine dispersion.

In conclusion, the XRD investigation reveals that the successful catalyst is composed of a Zn-or iron modified support oxide and a nanostructured Cu particle that is generated from nanostructured precursor oxides. The choice of the precursor route and of the anion for the Cu source are critical synthesis parameters for obtaining the desired nanostructuring. In this way, the XRD analysis has given clear indications for the at first sight unclear catalytic performances reported earlier in chapter four. To elucidate more on the nature of modification of the support and of the Cu particles, other methods will be needed that identify more local properties of the compounds and do not require long range crystalline ordering which was clearly identified as absolutely detrimental for catalytic performance.

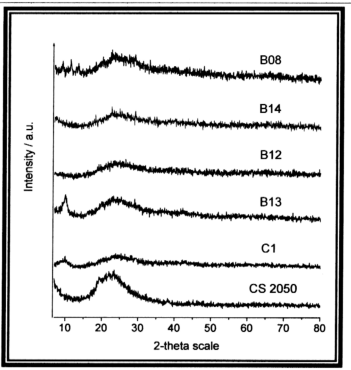

Figure 5.1: X-ray diffraction patterns of precursor Cu-Zn samples (including mono-copper sample) prepared via citrate-nitrate route. All precursors and bare support were dried in air at 383 K for 16 hours.

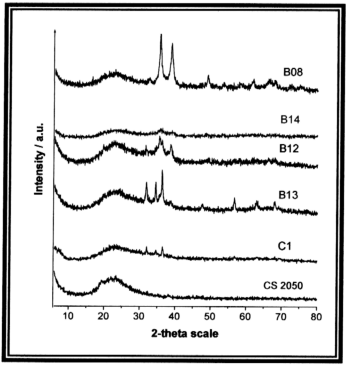

Figure 5.2: X-ray diffraction patterns of calcined Cu-Zn samples (including mono-copper sample) prepared via citrate-nitrate route. Calcined material and bare support were calcined in air at 723 K for 2 hours.

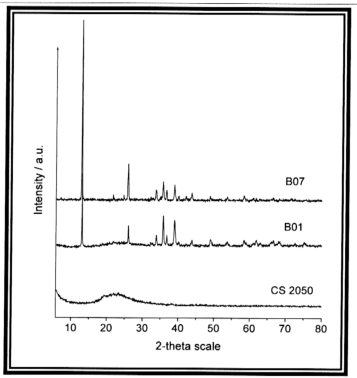

Figure 5.3: X-ray diffraction pattern of precursor Cu-Zn sample B07 prepared via nitrate route. Precursor and bare support were dried in air at 383 K for 16 hours.

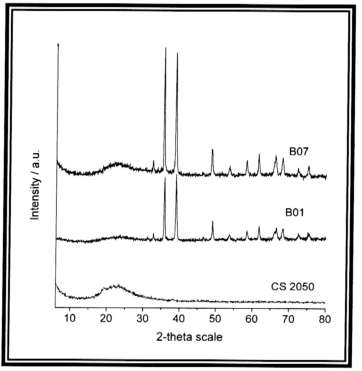

Figure 5.4: X-ray diffraction pattern of calcined Cu-Zn sample B07 prepared via nitrate route. Calcined material and bare support were calcined in air at 723 K for 2 hours.

Table 5.2: Characteristic of Cu-Zn samples after calcination.

Code	Main Peak	JCPDS	Observation
B08	35.85°, 38.95°, 48.96°, 66.20°, 68.31°	45-0937	Tenorite (syn), monoclinic lattice
C01	31.89°, 34.99°, 36.67°, 56.61°	36-1451	Zinc Oxide (zincite syn), hexagonal lattice
B12	32.07°, 34.58°, 35.09°, 36.45°	45-0937 36-1451	Lower intensity of Tenorite (copper oxide) and slight peak broadening. Overlapping of ZnO and CuO reflections.
B13	31.88°, 34.58°, 36.45°, 56.84°, 63.08°, 68.09°	45-0937 36-1451	Main peak of Tenorite (copper oxide) observed with more pronounced of ZnO refections.
B14	35.62°, 38.54°, 48.73°, 68.01°	45-0937	No reflection of ZnO, and very low intensity of tenorite.
B01	32.71°, 35.84°, 38.95°, 49.37°, 58.18°, 61.76°, 66.44°, 68.50°	45-0937	Highly crystalline material. Characteristic pattern assigned to tenorite (syn), monoclinic lattice.
B07	32.71°, 35.65°, 38.95°, 48.73°, 57.12°, 61.70°, 66.22°, 68.09°	45-0937	Highly crystalline material. Characteristic pattern assigned to tenorite (syn), monoclinic lattice. No indication of ZnO phase, probably due to the low loading.

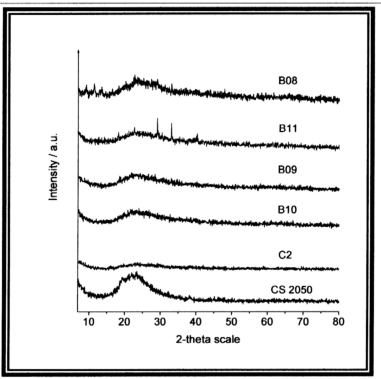

Figure 5.5: X-ray diffraction patterns of precursor Cu-Fe samples (including mono-copper sample) prepared via citrate-nitrate route. All precursors and bare support were dried in air at 383 K for 16 hours.

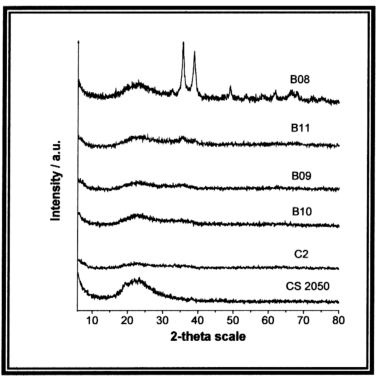

Figure 5.6: X-ray diffraction patterns of calcined Cu-Fe samples (including mono-copper sample) prepared via citrate-nitrate route. Calcined material and bare support were calcined in air at 723 K for 16 hours.

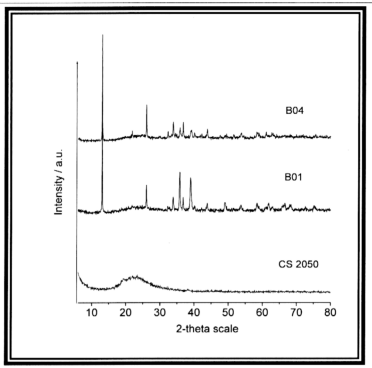

Figure 5.7: X-ray diffraction pattern of precursor Cu-Fe sample B04 prepared via nitrate route. Precursor and bare support were dried in air at 383 K for 16 hours.

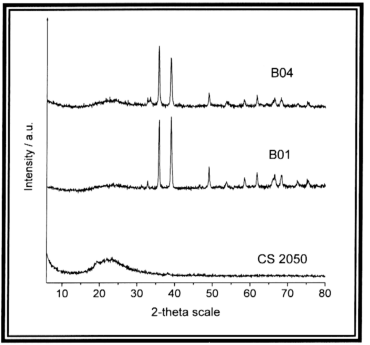

Figure 5.8: X-ray diffraction pattern of calcined Cu-Fe sample B04 prepared via nitrate route. Calcined material and bare support were calcined in air at 723 K for 2 hours.

Table 5.3: Characteristic of Cu-Fe samples after calcination.

Code	Main Peak	JCPDS	Observation
B08	35.85°, 38.95 °, 48.96°, 66.20°, 68.31°	45-0937	Tenorite (syn), monoclinic lattice
C2	-	-	Amorphous material
B09	-	-	Amorphous material
B10	-	-	Amorphous material
B11	-	-	Amorphous material
B01	32.71°, 35.84°, 38.95°, 49.37°, 66.44°,68.50°	45-0937	Highly crystalline material. Characteristic pattern assigned to tenorite (syn), monoclinic lattice.
B04	32.70°, 32.69°, 38.52°, 49.15°, 58.31°, 61.76°	45-0937	Highly crystalline material. Characteristic pattern assigned to tenorite (syn), monoclinic lattice. No indication of Fe_2O_3 phase, probably due to the low loading.

Table 5.4: Main diffraction peaks related to CuO (JCPDS 45-0937)

Plane	Diffraction angle (2θ)	Intensity
[-110]	32.497	8
[-111]	35.496	100
[111]	38.731	91
[-202]	48.727	20
[202]	58.377	9
[-113]	61.535	15
[-311]	66.250	11
[-220]	68.091	11

Table 5.5: Main diffraction peaks related to ZnO (JCPDS 36-1451)

Plane	Diffraction angle (2θ)	Intensity
[100]	31.770	57
[002]	34.422	44
[101]	36.253	100
[110]	56.603	32

5.1.2. Surface Area Measurement

The textural properties of catalyst support, precursors of the best samples of each series and calcined materials were determined using nitrogen adsorption techniques. Emphasis has been given to the best sample B14 and B11. The SIWI precursor and calcined material of B14 and B11 (*i.e.*, A14 and A11) were also measured. The results are summarized in Table 5.7 and depicted in Figure 5.10-5.13. Following this, the specific surface area, pore volume and average pore size distribution of all calcined samples in the Cu-Zn and Cu-Fe series were measured and depicted in Figure 5.14-5.19 and summarized in Table 5.8.

Based on IUPAC nomenclature, typical type IV isotherms were obtained for the pristine support silica and for all samples. For the silica support (Figure 5.9) there are four distinct regions seen in the graph (Table 5.6). The adsorption data in the range of P/P_0 0.05-0.30 are used for the calculation of the surface area of the material using Brunauer, Emmett and Teller (BET method). The measured surface area of silica support material is 521.11 m^2g^{-1} while its pore volume is 2.56 cm^3g^{-1}. From the isotherm curves, pore size distributions has been calculated according to the method of Barrett, Joyner and Halenda (BJH method). This method is appropriate to study changes of pore diameters upon catalyst preparation. A broad pore size distribution with pore size maxima at 160 Å is obtained for the silica support in agreement with the shape analysis of the isotherm. It can be concluded that the bare support silica is mesoporous material and exhibits a significant volume fraction of interparticle voidage. This characteristic of material is highly suitable for the preparation of impregnated catalyst systems. It is a major target to preserve this texture after the catalyst metal loading.

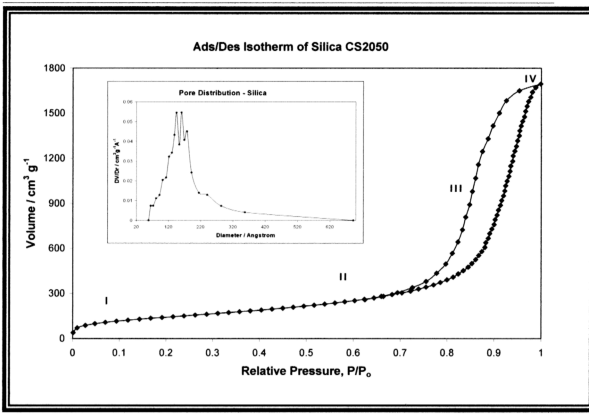

Figure 5.9: Nitrogen adsorption-desorption isotherms of silica support (CS 2050). Also (inset) th pore distribution of silica.

Table 5.6: Observation of nitrogen adsorption isotherm by region in bare silica support.

Region	Observation
I	Formation of monolayer adsorbate at the geometric surface of a material free of micropores.
II	At relative nitrogen pressure of approximate 0.54, exponential increase of the amount of adsorbed nitrogen caused by multiple condensation of nitrogen inside the mesopores.
III	Filling of mesopores of various sizes up to relative nitrogen pressure to 0.90.
IV	Relative pressure close to 1, ambigious and could be attributed to condensation of nitrogen within the interstitial voidage between the support particles and/or due to macroporosity presence in material.

[Ertl, G. *et al.*, 1997c]

It is the purpose of the investigation to detect textural changes of the parent support silica. These may originate from a chemical transformation of their basic structural units (incorporation of metal ions into the oxide matrix). In addition, the agglomeration of the basic structural units may change through precipitation of active metal oxide particles and or through modifications of the support oxide surfaces occurring from their contact with the impregnating liquid. The working hypothesis for the present analysis is that the well performing samples B14 and B11 were transformed in a stage where a modified support stabilized active metal (oxide) particles. All other samples failed to stabilize the active species as small particles or may even incorporate the active metal into the support.

Representative isotherms of the catalyst precursors and calcined material after 1st loading and 2nd loading are depicted in Figure 5.10-5.11 (B14) and Figure 5.12-5.13 (B11). It is observed that the general shape of the silica adsorption isotherm was preserved especially in samples after calcination. Nevertheless, the surface area as well as the pore volume is drastically reduced upon loading of metal precursors as observed in all precursor samples. This is a clear indication that not impregnation of the outer surface but precipitation has occurred during metal component loading as mesopores are large enough not to be blocked when their walls are covered with a layer of metal citrate complexes. Presumably after precursors loading, large amounts of copper ions were driven out of the mesopores with the solvent flow during drying treatment. As such, these copper particles have precipitated at or next to the external surface and the internal surface during drying, thus giving rise to the formation of small copper oxide particles during calcination. The complexes seemed to have formed a continuous layer of material encapsulating much of the support aggregates as the loss of surface area was drastic in all cases.

Table 5.7: Nitrogen adsorption-desorption analysis for precursor and calcined samples of A14, B14, A11 and B11.

Code	Composition	Precursor Sample			Calcined Sample		
		S_{BET} [a]	PV_{max} [b]	P_r [c]	S_{BET} [a]	PV_{max} [b]	$P_{r,max}$ [c]
A14	Cu-Zn at/at 3:1	87.09	0.23	69.9	234.79	0.76	104.5
B14	Cu-Zn at/at 3:1	58.21	0.15	41.0	286.96	0.79	71.0
A11	Cu-Fe at/at 3:1	53.40	0.16	61.1	282.30	0.84	65.3
B11	Cu-Fe at/at 3:1	25.32	0.12	34.1	235.48	0.68	51.5

[a] Specific Surface Area, ($m^2 g^{-1}$)
[b] Pore Volume, ($cm^3 g^{-1}$)
[c] Pore size distribution maximum, (Å)

After calcination (in regardless during 1st impregnation or 2nd impregnation), the profile of silica is not fully recovered and a narrower pore size distribution is observed. No broadening of the samples pore size distribution which will typically indicating extensive damages of the silica original framework was observed in all cases. The pore volume has significantly decreased in tandem with specific surface area, most typically due to pore filling by metal oxide and / or pore blocking.

The reduction in textural parameters is substantial with respect to those of the pristine supports. The fact that much of the reduction in surface area is reversed upon calcination strongly underlines that leaching and etching of the support oxide by the complexating metal ion solutions cannot be the dominating processes. The data in Table 5.7 underline that the pore blocking species was destroyed during calcination. Most if not all citrates-nitrate crystallites should have converted into the respective metal oxides. This process would be expected to follow a cracking-core-and-shell mechanism as it is conducted under temperature-programmed condition. Consequently, many very tiny oxide particles will be supported on the silica.

It was evident from the XRD measurements that copper oxide reflections were almost absent in calcined samples B14 and B11, the one remaining having very low intensity and being very broad indicating that the copper oxide present must be very small. The shape change of the isotherms in Figure 5.11 and 5.13 for the catalysts with respect to the pure support clearly reveals the significant blocking of the mesopore volume through the loaded oxide particles by the modification at high p/p_o values. The restoration of part of this volume is accompanied by significant increase of the intergranular void space of the macroscopic particles as evidenced by the spike in adsorbed volume close to $p/p_o = 1$. One expects rough particles of irregular shape and surface texture.

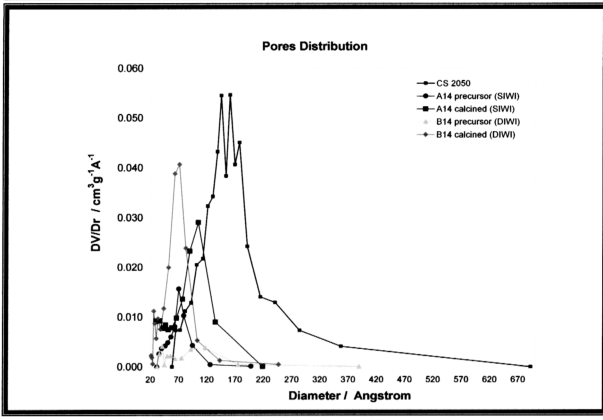

Figure 5.10: Pore Size Distribution of A14 and B14; precursor and calcined samples.

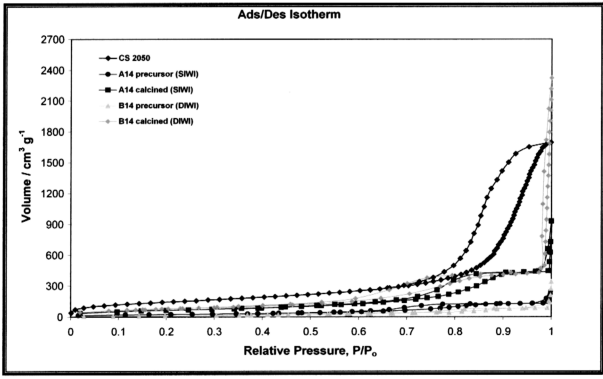

Figure 5.11: Nitrogen adsorption-desorption isotherm of A14 and B14; precursor and calcined samples.

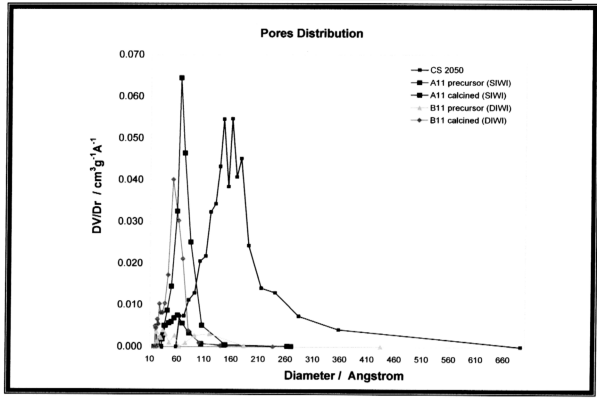

Figure 5.12: Pore Size Distribution of A11 and B11; precursor and calcined samples.

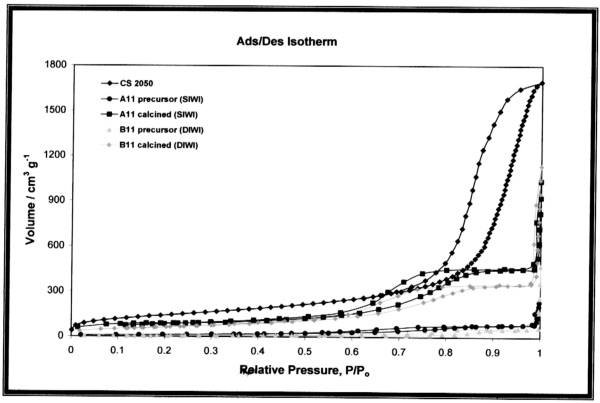

Figure 5.13: Nitrogen adsorption-desorption isotherm of A11 and B11; precursor and calcined samples.

Table 5.8: Nitrogen adsorption-desorption analysis of all samples in Cu-Zn and Cu-Fe series after calcination. Highlighted in blue are the sample prepared via nitrate route, precursor P1.

Code (calcined)	Composition	Precursor	S_{BET} [a]	PV_{max} [b]	P_r [c]
B01	Mono-Cu	P1	21.06	0.07	71.6
B07	Cu-Zn at/at 3:1	P1	190.81	0.64	79.6
B04	Cu-Fe at/at 3:1	P1	213.88	0.88	129.1
B08	Mono-Cu	P2	391.36	0.89	67.7
B12	Cu-Zn at/at 1:1	P2	158.46	0.55	52.6
B13	Cu-Zn at/at 1:3	P2	174.29	0.57	61.1
B14	Cu-Zn at/at 3:1	P2	286.96	0.79	71.0
B09	Cu-Fe at/at 1:1	P2	330.83	0.98	91.7
B10	Cu-Fe at/at 1:3	P2	304.52	0.79	83.0
B11	Cu-Fe at/at 3:1	P2	235.48	0.68	51.5

[a] Specific Surface Area, ($m^2 g^{-1}$)
[b] Pore Volume, ($cm^3 g^{-1}$)
[c] Pore size distribution maximum, (Å)

Representative pore distribution curves and isotherms of the samples prepared by precursor P1 after loading and calcination are given in Figure 5.14 and Figure 5.15. The shocking loss of surface area and pore volume of sample B01 is noted; this sample at the same time exhibited thick segregation of copper oxide as observed in SEM micrographs; both observations give the reason why this sample will not exhibit any catalytic potential. With the addition of zinc or iron (at/at 3:1) in samples B04 and B07, the pore distribution showed generally a small improvement as compared to sample B01. For the nitrate family of samples it is evident that the addition of iron led in general to a less drastic loss of texture than the addition of zinc, as can be concluded from inspection of Figure 5.15.

Figures 5.16-5.19 compiled the pore size distribution and adsorption-desorption isotherm of measured calcined Cu-Zn and Cu-Fe samples prepared via citrate-nitrate route. All specific surface areas measured for samples are typically lower than that of silica CS 2050 at 521.11

m^2g^{-1}, suggesting that the specific surface area loss had occurred after impregnation and calcination procedure (Table 5.8). All samples also exhibited consistently a clear decrease in average pore diameters relative to support. As mentioned, this could be related to the filling and/ or blocking of pores by CuO (oxides of 2^{nd} metal) particles. It is unfortunate however, that no relationship was found to exist between the copper content or influence of the addition of 2^{nd} metal to the overall surface area.

The specific surface area and average pore diameter changes in parallel with the different composition of metal solutions used. It is worthwhile to point out that the original structure of silica has not been recovered as some of the metals added have reacted with the support oxide by either dissolution and or compound formation in X-ray amorphous forms. The trend in which the decrease of specific area observed from sample B14 (Cu-Zn at/at 3:1), B13 (Cu-Zn at/at 1:3) to B12 (Cu-Zn at/at 1:1) of the Cu-Zn series correlates well with their catalytic behavior, *i.e.*, the higher surface area resulted in higher catalytic activity. On the other hand, mono-copper catalyst B08 prepared using the same precursor P2, which exhibited the highest surface area measured at 391.36 m^2g^{-1} yields inferior catalyst as compared to catalyst B14 by approximately 30% (yield) and B11 by approximate 12% (yield). Lower activity of B08 was ascribed to the lacking in degree of active metal dispersion and homogenity, owing likely to the absence of a small quantity of 2^{nd} metal zinc or iron modifying the support as to accommodate highly disperse Cu particles. The data show clearly that a combination of high loading and of high dispersion are the characteristic parameters for well-performing catalysts. The data also clearly support the notion that the non Cu metal addition has the function of a structural promoter through modifying the silica support.

No discernible trend was found to relate the specific surface area to the catalytic activity of catalyst from the Cu-Fe binary series (at/at 1:1, 1:3, and 3:1). Contrary to Cu-Zn catalysts, the best Cu-Fe catalyst B11 prepared via nitrate-citrate route exhibited the lowest specific surface area. Here it seems possible that the silica acted just as a support for a dense layer of iron oxide blocking the mesopore volume but providing the bed for small Cu particles that are fully supported on iron oxide. The much higher propensity of iron oxo-precursors to form layers or crystals with each other through olation-oxolation [Livage J., 1998] in the drying process as compared to the Zn compounds that easily dissolve into silica substrate is the chemical origin for this apparent difference in function of the non-Cu metal: Zn as modifier, Fe as structure-former both provide the immediate contact for highly active small CuO/Cu particles.

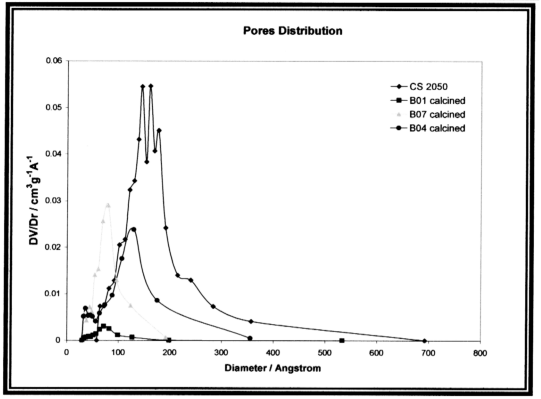

Figure 5.14: Pore Size Distribution of calcined samples prepared via nitrate route (precursor P1).

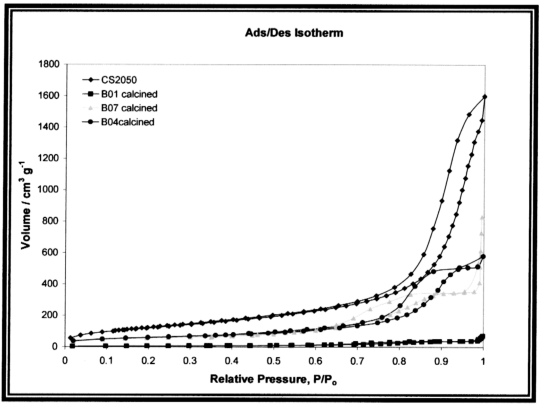

Figure 5.15: Nitrogen adsorption-desorption isotherm of calcined samples prepared via nitrate route (precursor P1).

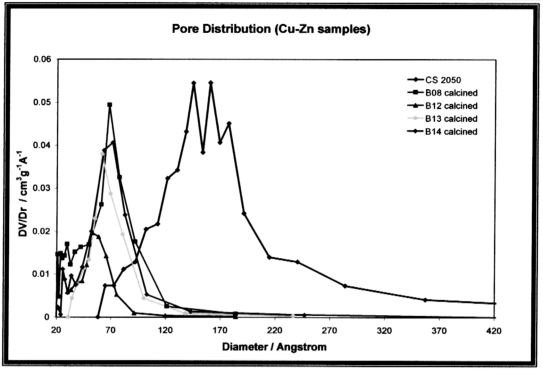

Figure 5.16: Pore Size Distribution of Cu-Zn calcined samples prepared via citrate-nitrate route (precursor P2).

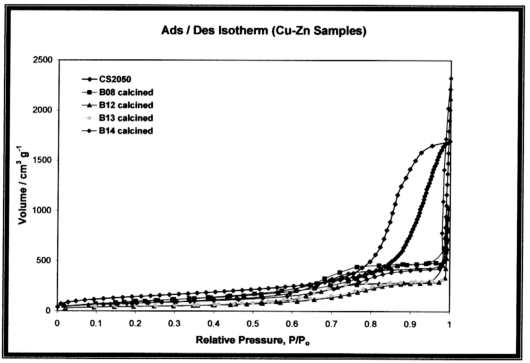

Figure 5.17: Nitrogen Adsorption - Desorption Isotherm of Cu-Zn calcined materials prepared via citate-nitrate route (precursor P2).

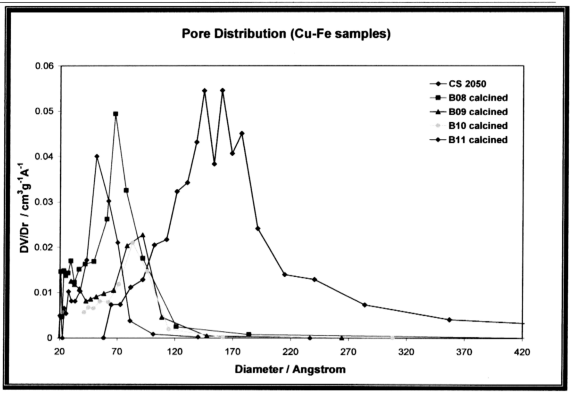

Figure 5.18: Pore Size Distribution of Cu-Fe calcined samples prepared via citrate-nitrate route (precursor P2).

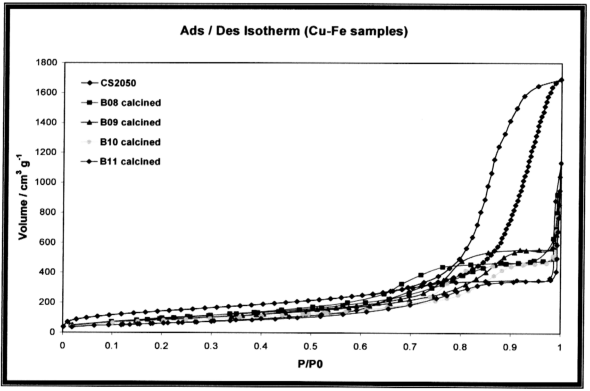

Figure 5.19: Nitrogen Adsorption - Desorption Isotherm of Cu-Fe calcined materials prepared via citate-nitrate route (precursor P2).

5.1.3. SEM and EDX: Structural and Morphology Study

The samples represent formally "impregnated" systems. From the amount of loading and the preparation methods it is obvious that the materials are in fact more diluted precipitates with a substantial bulk character of the deposited material rather than a support phase with clusters of deposits on the surface of the crystallites. The technique of SEM is useful to study the micro morphology in addition to the more integral examination by BET. EDX allows further identification of the chemical nature of mesoscopic objects.

If a number of local EDX analyses are averaged, it should be possible to verify the integral chemical composition of the samples. This was done by analyzing five spots on each material and the results are summarized in Table 5.9. Individual analysis results are reported in the results part. From these data it can be seen how vastly different the local composition can be from an average sample content. This underlines the multiphasic nature of the samples. It is not trivial to elucidate this point in materials that are fully X-ray amorphous. With electron microscopy alone it is also difficult to find the typical structure of a complex material. Together with the data presented so far, it is possible to augment analysis of the picture derived so far by SEM-EDX data without falling into the problem of selecting the "typical" situation.

The deviations between theoretical and experimental composition arise from several sources of error. The systematic error of the EDX method can be estimated to be 3 wt%. A larger source of error arises from the varying electronic structure of the samples giving rise to vastly different volumes of analysis at different locations in the same sample (interaction profile of the electron beam with different electronics structures). Finally, the

compositional variation in the samples is so large that an average of 5 sampling points may not be sufficient for eliminating the fluctuations. Taking all these considerations into account it can be stated that in all samples the agreement between theoretical and experimental composition is good to fair. Large deviations indicate large textural fluctuations. For this reasons it was not found adequate to statistically analyze the data and quote the standard deviations as a measure of accuracy.

Therefore SEM inspection and 5-spots EDX measurement were carried out on bare support silica and all calcined materials. Results were processed and depicted from Figure 5.20 – 5.42 and tabulated in Table 5.9. Alongside samples, SEM micorgraphs of reference samples C1 and C2 (mono-zinc and mono-iron supported on silica) were also captured.

Table 5.9: Averages of EDX measurements on samples

Samples	Weight % of Cu		Atomic % of Cu		Weight % of M2		Atomic % of M2		Total Weight % of Metal		Total Atomic % of Metal	
	cal.	exp.	cal.	exp.	cal.	exp.	cal.	exp.	cal.	exp.	cal.	exp.
B01	41.02	40.88	17.70	17.25	0.00	0.00	0.00	0.00	41.02	40.88	17.70	17.25
B07	29.56	28.14	12.90	11.91	10.12	10.14	4.27	4.94	39.68	38.28	17.17	16.85
B04	25.36	25.15	10.50	9.60	7.46	6.95	3.43	2.52	32.82	32.10	13.93	12.11
B08	28.81	28.06	11.20	10.45	0.00	0.00	0.00	0.00	28.81	28.06	11.20	10.45
B12	14.06	14.59	5.50	5.20	14.43	12.08	5.51	4.19	28.49	26.67	11.01	9.39
B13	6.95	5.38	2.70	1.75	21.40	20.63	8.17	6.83	28.35	26.01	10.87	8.58
B14	21.35	20.65	8.30	7.36	7.30	6.54	2.79	2.25	28.65	27.19	11.09	9.60
B09	11.79	10.76	4.40	3.40	10.40	9.95	4.36	3.56	22.19	20.71	8.76	6.97
B10	5.46	5.45	1.90	1.56	14.47	5.92	5.94	1.92	19.93	11.37	7.84	3.48
B11	19.11	18.16	7.00	6.18	5.74	4.43	2.46	1.70	24.85	22.59	9.46	7.88

M2 = Fe or Zn
Cal. = Calculated value
Exp. = Experimental value obtained by averaging of EDX measurements

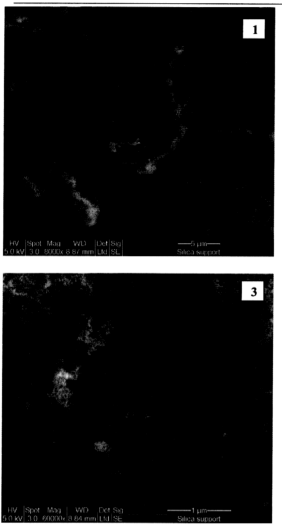

Figure 5.20: SEM-image of the CS 2050 silica, thermally pre-treated at 573 K *prior* to impregnation and subjected to the same thermal treatment as other catalysts *after* impregnation

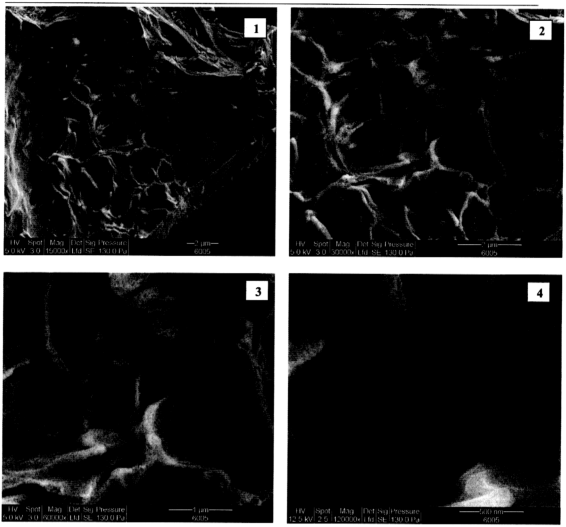

Figure 5.21: SEM-image of C1; calcined at 723K.

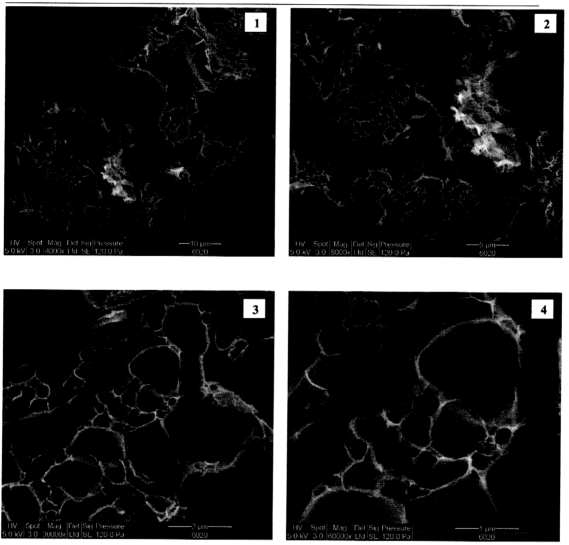

Figure 5.22: SEM-image of C2; calcined at 723K.

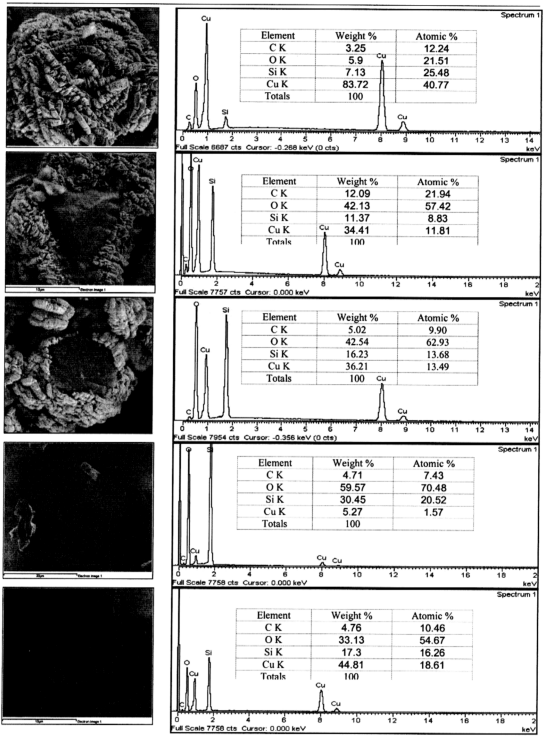

Figure 5.23: EDX of the calcined material B01. Calcination temperature at 723K.

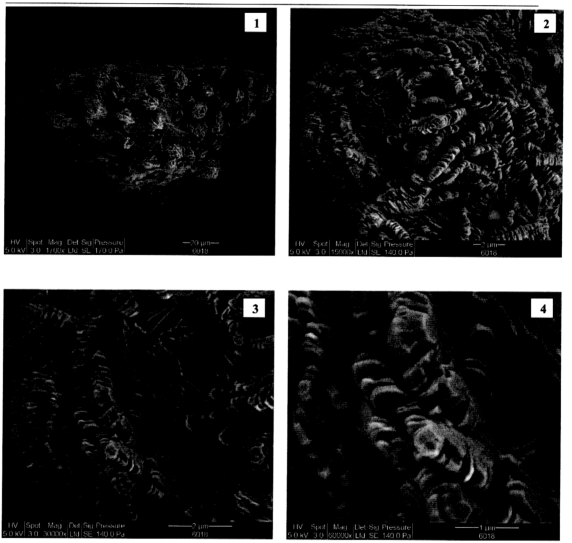

Figure 5.24: SEM-image of B01; calcined at 723K.

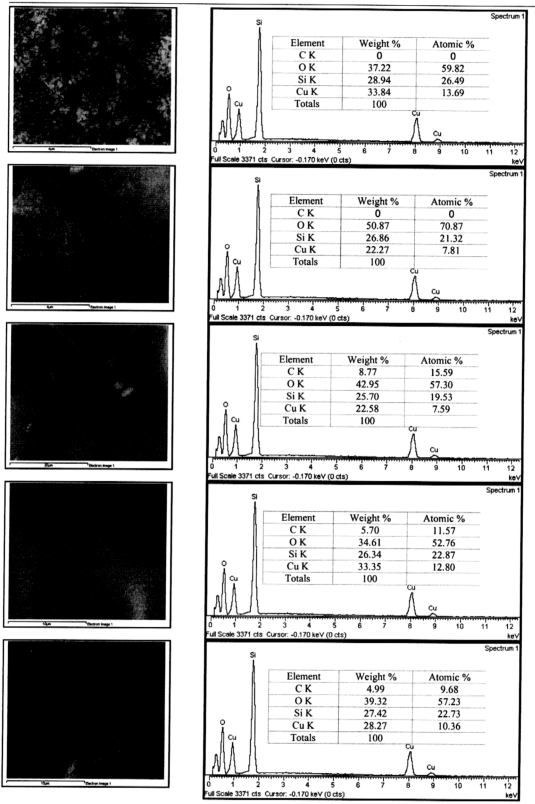

Figure 5.25: EDX of the calcined material B08. Calcination temperature at 723 K.

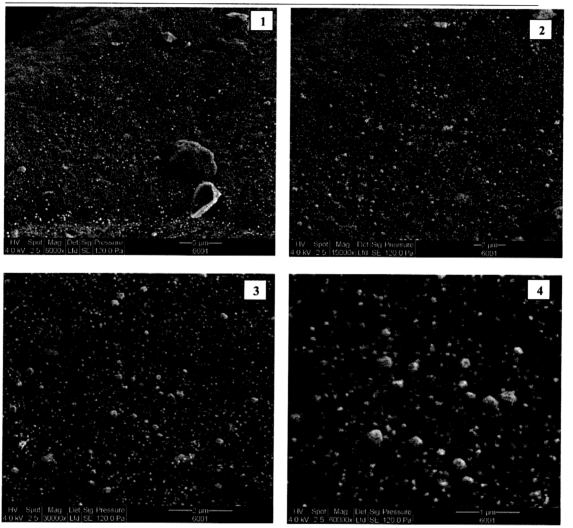

Figure 5.26: SEM-image of B08; calcined at 723K.

The micrographs of calcined silica as exhibited in Figure 5.20 showed the agglomerates of platelets network that appeared most fluffy (cloud-like). The large depth of contrast with the medium voltage 5 keV indicates that the aggregates of this sample are highly porous; mesoporous as indicated from the nitrogen adsorption measurement. Micrographs of reference C1 (mono-zinc) and C2 (mono-iron) show similar compact morphology as depicted in Figure 5.21 and 5.22. The illustration of Zn and Iron oxide particle in bubble structure due to film decomposition of ligand is observed.

In Figures 5.23-5.26 the reference materials Cu-only prepared via P1 and P2 protocols are compared for their morphology and textures. It is obvious that the nitrate method gave rise to much coarser agglomerations of precipitates than the citrate method. At the resolution chosen to yield adequate EDX data the mesoporosity of the support was not resolved. The homogeneous contrast of the "smooth" patches is, however a good indication that these areas are homogeneously covered by precipitates. Bare support should exhibit a small-scale texture arising from the agglomerates of the basic structural units. The lower two plates especially in both Figures 5.23 and 5.25 expose such bare support areas. A large amount of active oxides is found in large aggregates of agglomerated crystals being shown in the top two plates of each Figure (5.23 and 5.25). Such a texture is detrimental for catalytic performance and should be avoided under all circumstances. This morphology is a clear indication that the active material had no fixation to the support during its geneses and behaved like a fused precipitate diluted by the support oxide. The fact that in both Figures also small scale structures were detected with different morphology of the aggregates is an indication that some of the precursor was bonded to the support during its chemical transformation. The higher granularity of the sample prepared via P1 arises from the mesophase state in which the nitrate-hydroxide is liquid and forms droplets anchoring at uneven patches of the support aggregate. It is evident that method P2 is much superior in providing a chance for finely divided Cu oxide structures on the support. The structuring clearly explains the catalytic performance for which P1 is much inferior than P2 with the same nominal loading.

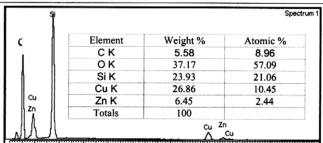

Element	Weight %	Atomic %
C K	5.58	8.96
O K	37.17	57.09
Si K	23.93	21.06
Cu K	26.86	10.45
Zn K	6.45	2.44
Totals	100	

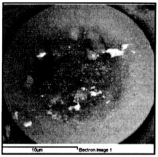

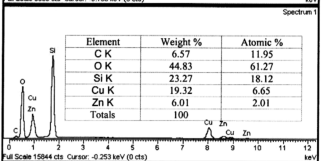

Element	Weight %	Atomic %
C K	6.57	11.95
O K	44.83	61.27
Si K	23.27	18.12
Cu K	19.32	6.65
Zn K	6.01	2.01
Totals	100	

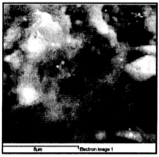

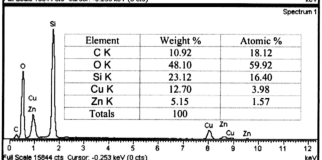

Element	Weight %	Atomic %
C K	10.92	18.12
O K	48.10	59.92
Si K	23.12	16.40
Cu K	12.70	3.98
Zn K	5.15	1.57
Totals	100	

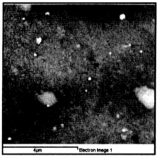

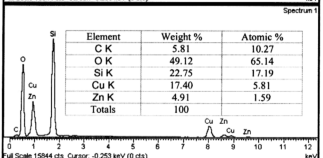

Element	Weight %	Atomic %
C K	5.81	10.27
O K	49.12	65.14
Si K	22.75	17.19
Cu K	17.40	5.81
Zn K	4.91	1.59
Totals	100	

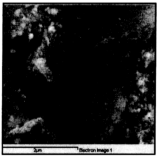

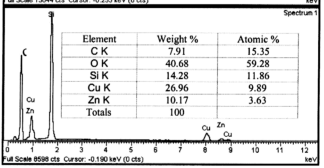

Element	Weight %	Atomic %
C K	7.91	15.35
O K	40.68	59.28
Si K	14.28	11.86
Cu K	26.96	9.89
Zn K	10.17	3.63
Totals	100	

Figure 5.27: EDX of the calcined material B14: Calcination temperature at 723 K.

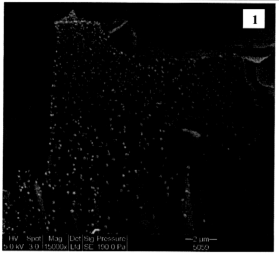

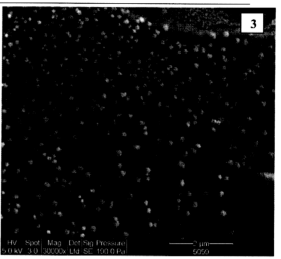

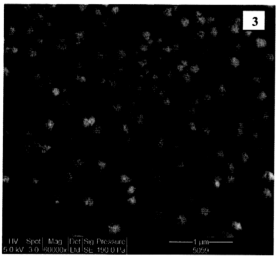

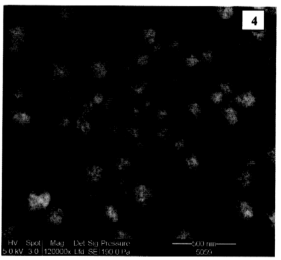

Figure 5.28: SEM-image of B14; calcined at 723K.

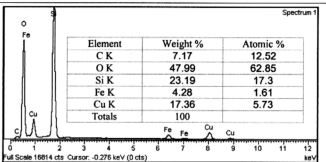

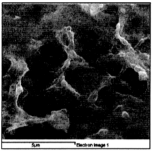

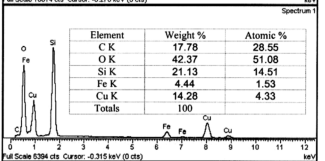

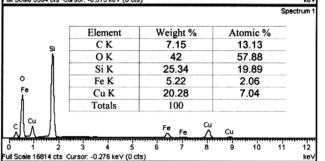

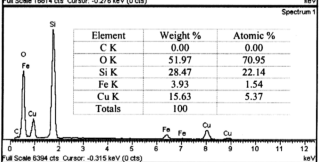

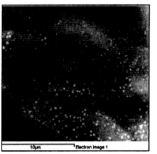

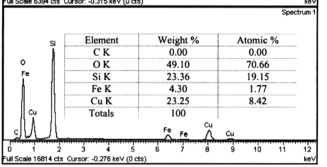

Figure 5.29: EDX of the calcined material B11: Calcination temperature at 723 K.

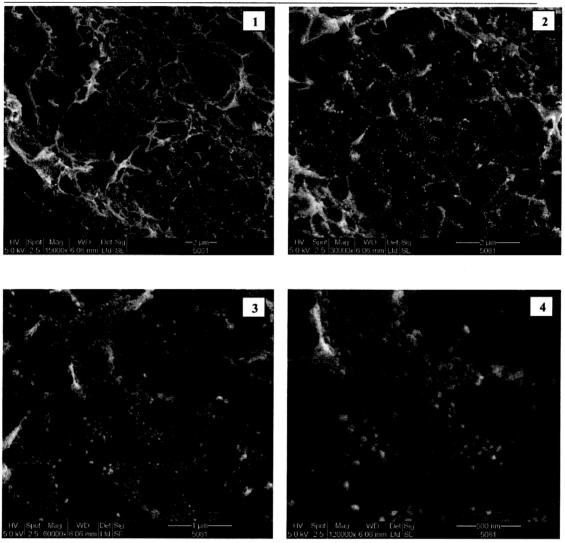

Figure 5.30: SEM-image of B11; calcined at 723K.

The catalytically best samples from the zinc and iron families are compared in Figures 5.27 to 5.30. It is immediately obvious that in both samples the nominal content in active metals seems to be low in the EDX spectra but it also occurs that it is very evenly distributed. In fact, the content is close to the expected values and the standard deviation between these spectra was small compared to all other spectra. The images reveal small aggregates of active oxides on large superstructures of support aggregates. The superstructure is reminiscent on petrified form indicating the strong restructuring

associated with the drying citrate solution acting as surfactant for the aggregates of the support oxides.

In the high resolution images (bottom of both Figures 5.27 and 5.29) the aggregated Cu oxides can be seen as small particles sitting isolated but well supported on the coarse structure of the modified support. The extent of modification by incorporation of Zn or by deposition of an iron oxide layer is barely visible in the images. It is evident that the morphology of the Cu oxide particles is the most relevant factor for preparing a successful catalyst. It can be understood from these observations how important the modification of the silica is if one compares the Figures 5.27, 5.28 with 5.25, 5.26. On bare support the Cu precursors are so finely divided that they cannot be resolved as individual clusters under the conditions of EDX imaging. On the successful catalysts the copper oxide forms aggregates which expose their activated surface much better to the gas phase than in the monometallic systems. It can be said that the utilization of the Cu in the modified support systems is much superior to that of the monometallic systems. This is a morphological explanation of the effect of the second element that fits well with the kinetic and spectroscopic information which all point to such a textural or structural rather than to an electronic or alloying function of the second element. The nature of this element Zn or Fe cannot be distinguished from the morphology of both the modified support nor from the active particles.

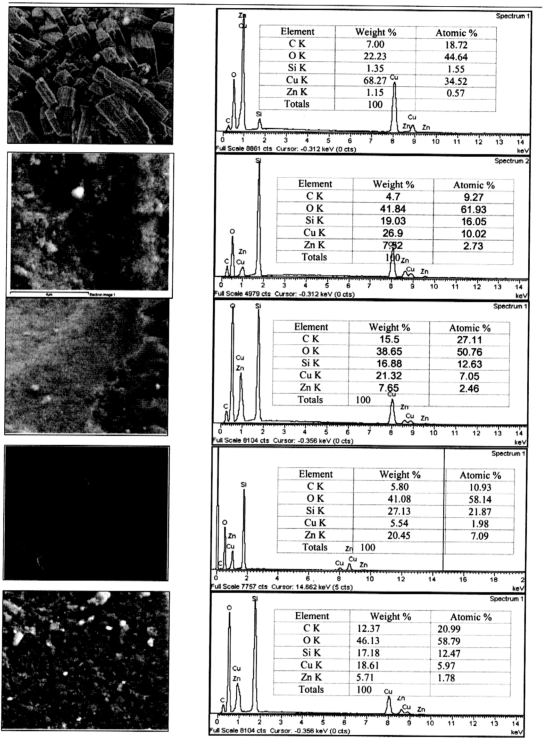

Figure 5.31: EDX of the calcined material B07. Calcination temperature at 723K.

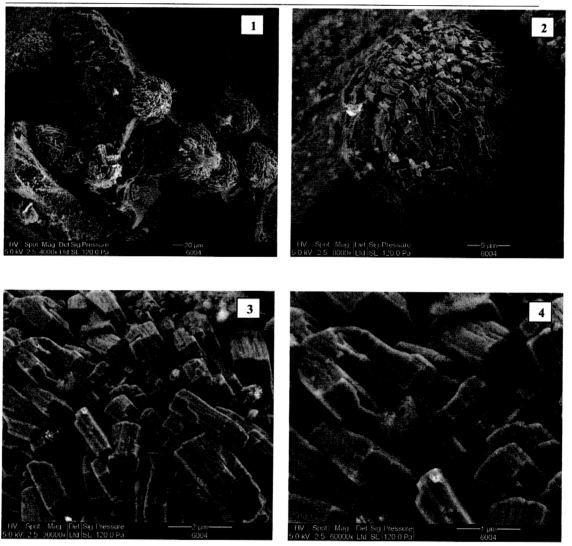

Figure 5.32: SEM-image of B07; calcined at 723K.

The choice of the synthesis protocol is also extremely relevant for controlling the morphology. In Figure 5.31 the sample with the same composition as in Figure 5.27 is shown. Whereas 5.27 shows B14 made after P2 the Figure 5.31 shows sample B07 made after P1. The typical texture is coarse with large aggregates of active oxides grown into crystalline morphologies. It is no surprise to expect X-ray diffraction patterns from such crystals of a tenorite. It is probably the mesophase state of the molten nitrate salt that is so detrimental for the dispersion of the active oxide. In some patches (central 3 plates) the kinetics of decomposition was fast enough to prevent the mesophase from collapsing before the nitrate was decomposed. This means that the

control of synthesis kinetics is in P1 so much more difficult than in P2 where the auto-explosion of the ligand helps greatly to achieve dispersion and the absence of a mesophase renders the temperature program much less critical than in the P1 approach.

The micromorphology of B04 (Figure 5.33 and 5.34) formation of rosettes of platelets very reminiscent of iron oxyhydroxide carrying large amounts of Cu oxide. Such structures which are secondary to the support are also detrimental as they prevent the dispersion of the Cu apparently by formation of iron-copper oxide interactions. As all these features are X-ray amorphous it is hard to assign possible structures to these rosettes. It is evident that they are to be avoided in successful catalyst preparations.

The samples presented in Figures 5.35-5.42 have all in common that massive restructuring of the previously compact support agglomerates have occurred. All samples are rich in the modifying element M2 and were prepared by the P2 protocol. Zn or Fe modification plus the surfactant effect of the drying citric acid seem to be very effective in dismantling and restructuring the support phase. In all samples only very few of the small Cu oxide aggregates are found that were characteristic of the active samples B14 and B11. It can be concluded that not enough copper material was put into the synthesis and that the process of restructuring the support seems to occlude the Cu that is present in EDX without exposing a discernible micromorphology. All compositions with relatively high abundances of the modifier element M2 seem to be detrimental for structure and thus for catalytic performance. The images exemplify that the micromorphology is closely related to the action of the modifier element that is not Cu but to the synthesis protocol. Uniform characteristics of effective and inefficient catalysts can be derived from both SEM images and EDX variances throughout a given sample.

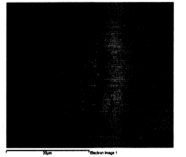

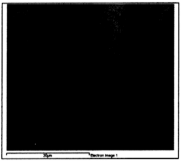

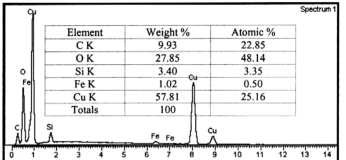

Element	Weight %	Atomic %
C K	9.93	22.85
O K	27.85	48.14
Si K	3.40	3.35
Fe K	1.02	0.50
Cu K	57.81	25.16
Totals	100	

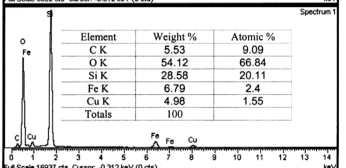

Element	Weight %	Atomic %
C K	5.53	9.09
O K	54.12	66.84
Si K	28.58	20.11
Fe K	6.79	2.4
Cu K	4.98	1.55
Totals	100	

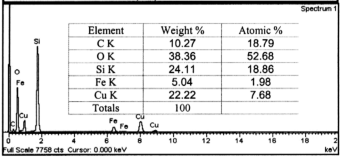

Element	Weight %	Atomic %
C K	10.27	18.79
O K	38.36	52.68
Si K	24.11	18.86
Fe K	5.04	1.98
Cu K	22.22	7.68
Totals	100	

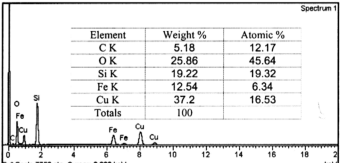

Element	Weight %	Atomic %
C K	5.18	12.17
O K	25.86	45.64
Si K	19.22	19.32
Fe K	12.54	6.34
Cu K	37.2	16.53
Totals	100	

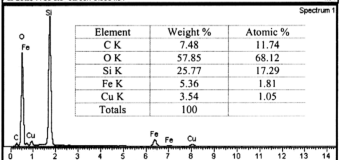

Element	Weight %	Atomic %
C K	7.48	11.74
O K	57.85	68.12
Si K	25.77	17.29
Fe K	5.36	1.81
Cu K	3.54	1.05
Totals	100	

Figure 5.33: EDX of B04; calcined at 723 K.

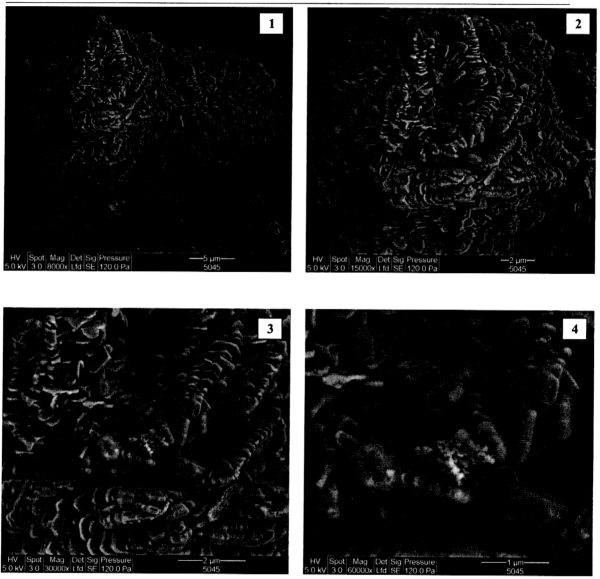

Figure 5.34: SEM-image of B04; calcined at 723K.

Spectrum 1

Element	Weight %	Atomic %
C K	7.26	14.36
O K	37.55	55.76
Si K	19.94	16.86
Cu K	19.02	7.11
Zn K	16.23	5.90
Totals	100	

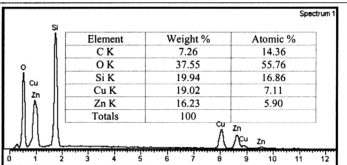

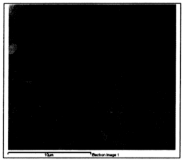

Spectrum 1

Element	Weight %	Atomic %
C K	6.21	11.83
O K	40.12	57.35
Si K	25.58	20.83
Cu K	15.28	5.5
Zn K	12.81	4.48
Totals	100	

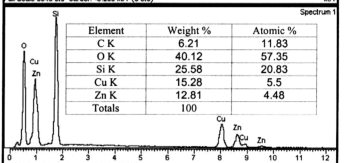

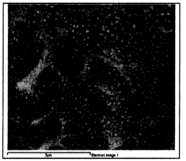

Spectrum 1

Element	Weight %	Atomic %
C K	8.66	17.15
O K	33.4	49.69
Si K	24.57	20.82
Cu K	18.22	6.82
Zn K	15.15	5.51
Totals	100	

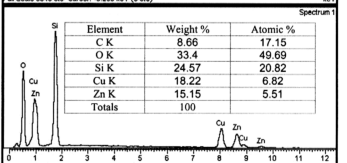

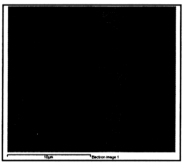

Spectrum 1

Element	Weight %	Atomic %
C K	7.50	12.64
O K	50.87	64.37
Si K	24.34	17.55
Cu K	10.06	3.21
Zn K	7.23	2.24
Totals	100	

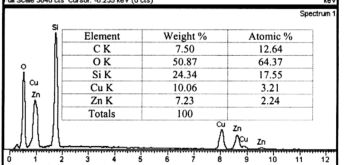

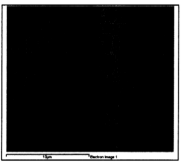

Spectrum 1

Element	Weight %	Atomic %
C K	7.5	12.64
O K	50.87	64.37
Si K	24.34	17.55
Cu K	10.06	3.21
Zn K	7.23	2.24
Totals	100	

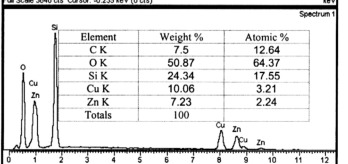

Figure 5.35: EDX of B12; calcined at 723 K.

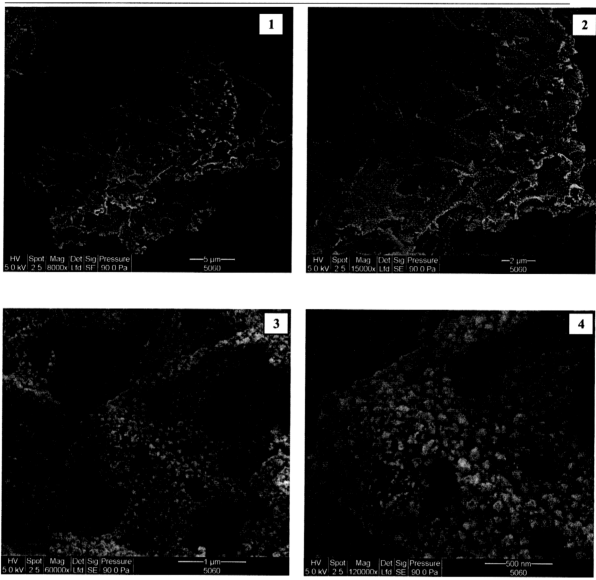

Figure 5.36: SEM-image of B12; calcined at 723K.

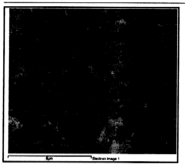

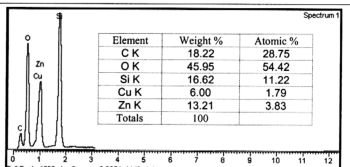

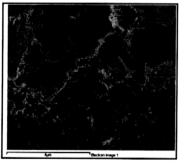

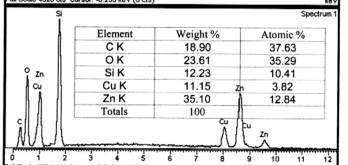

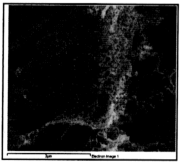

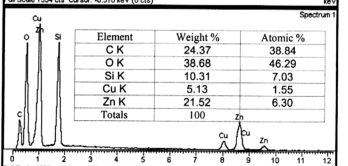

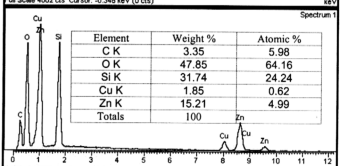

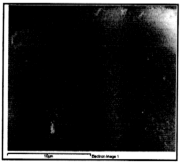

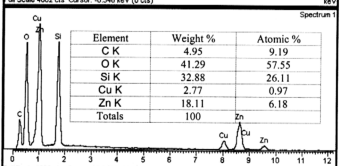

Figure 5.37: EDX of B13; calcined at 723 K.

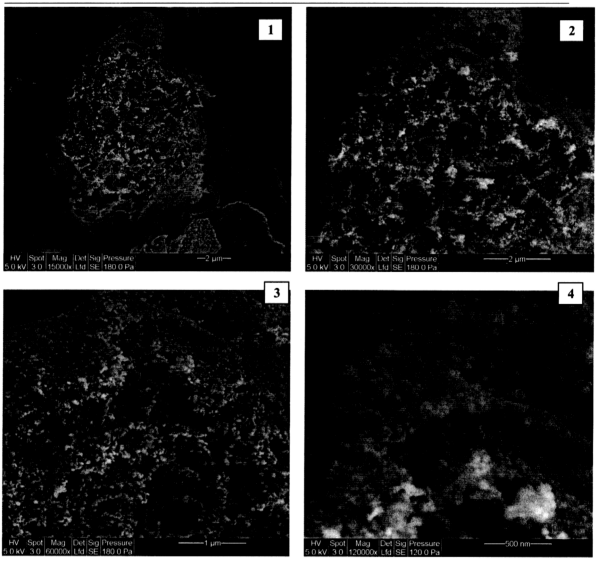

Figure 5.38: SEM-image of B13; calcined at 723K.

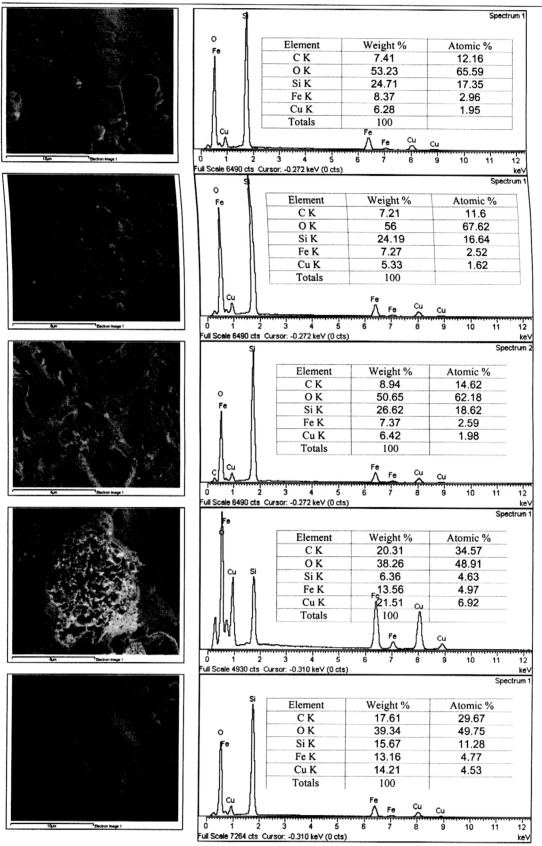

Figure 5.39: EDX of B09; calcined at 723 K.

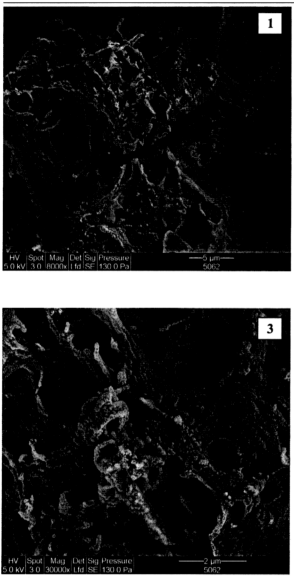

Figure 5.40: SEM-image of B09; calcined at 723K.

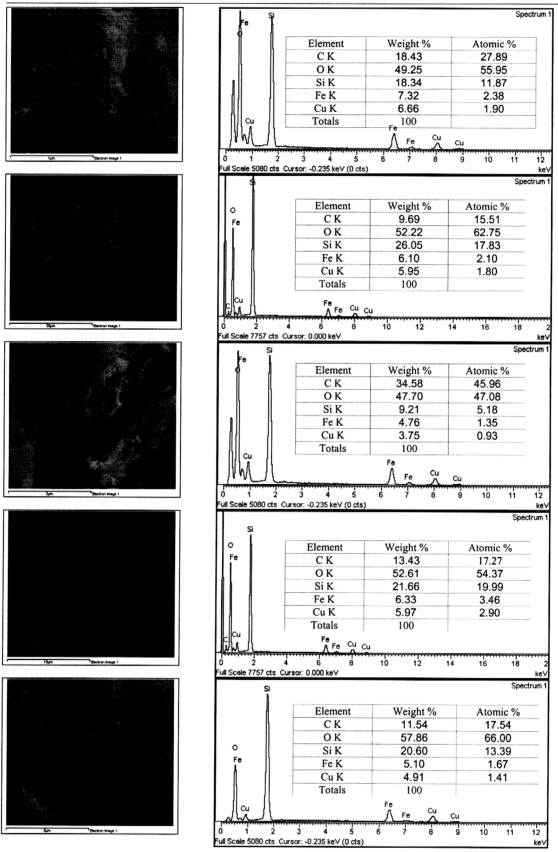

Figure 5.41: EDX of B10; calcined at 723 K.

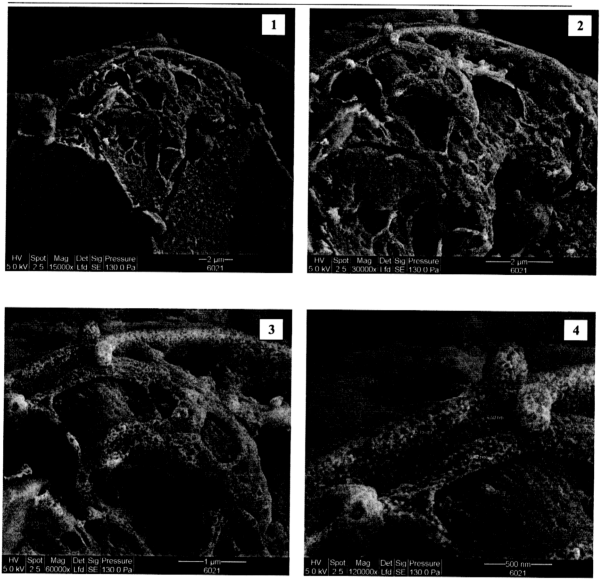

Figure 5.42: SEM-image of B10; calcined at 723K.

5.1.4. UV-Vis characterization

Diffuse Reflectance (DR) UV-Vis spectroscopy was used to investigate the state of the cations in all precursor and calcined samples. Bare support silica (CS 2050), copper nitrate (Alfa Aesar, 98%), copper citrate (Pfaltz and Bauer, 98.9%) and copper oxide (Aldrich, 99.0%) were also measured as guidance in interpretation work of samples data (Appendix G).

In truth, DR-UV Vis is a suitable technique to quantify the apparent coloring of a sample. An example can be given with sample A14 which is blue in color; it exhibited the typical characteristic of the presence of cupric ions Cu^{2+} incorporated into silica; indicating that Cu cations are dispersed into silica matrix in a dilute form rather than forming a (crystalline) Cu-silicate phase. After the first calcination, A14 was dark grey in color, which suggests that CuO phase was formed [Z.Wang, et al, 2003]. After the 2nd impregnation, the resulting material B14 (precursor and calcined sample) were dark solids. Relatively different from Cu-Zn samples, the color of all Cu-Fe samples were all visibly dark/black, indicating the presence of mixed valence Fe^{2+}/Fe^{3+} oxides rather than of the expected ferric oxyhydroxides which are much lighter in color. Therefore, the reflected light intensity of the DR spectra from these samples is typically very poor as depicted in Figures 5.43-5.48.

The spectral range can be divided into two parts; 1000 nm-500 nm (visible range) and below 500 nm (UV range). Care must be taken to observe the representation of the spectra in reflectivity units in which maxima indicate minimum absorption and minima stand for strong absorptions. All bands are broad and diffuse indicating a significant structural disorder of all compounds involved which is well in line with the XRD

results. All the samples exhibited a broad and asymmetric absorption band (a.b) at 700 nm – 800 nm and sharp bands below 400 nm. The first band is assigned to d-d transition of Cu (II) cations and indicates the presence of Cu (II) ions located in an octahedral environment. This d-d transition band is shifted towards lower wavelength (between 730-762 nm) as the copper loading increases in the samples (Figure 5.43). The second featured band below 350 nm can be ascribed to a ligand metal charge transfer (LMCT) band in clustered Cu(II) ions O^{2-}-Cu^{2+} [A. N Pestryakov *et al.*, 1996], [Z. R Ismagilov *et al.*, 2004], [A. N Pestryakov *et al.*, 2002], [O.V Komova, *et al.*, 2000], [A. N Pestryakov, *et al.*, 2004]. LMCT band at 299 nm indicating the presence of isolated Cu (II) and the LMCT band at higher wavelength indicating the presence of Cu(II) in clustered form. Generally, it was observed that the LMCT band differed significantly for the Cu-Zn samples; very likely attributed also by the varied Zn content.

After calcination (Figure 5.44), the spectra of Cu-Zn samples are dissimilar from the spectra of precursor samples. It was unfortunate that the poor reflectivity of the calcined samples excludes meaningful peak identification. As the best sample B14 exhibited the poorest reflectance, it can be concluded that a uniform coverage of the support with copper oxide particles destroyed the initial reflectivity. The coverage must thus be complete to account for the loss in coherent light scattering. Sample B13 which contained the highest amount of zinc compared to sample B12 and B14 was evidently not a good catalytic material since phase separation was observed. Sample B13 most likely contained zinc oxide alongside copper oxide and silica, as evidently observed from the dominating ZnO band at 311 nm. This was a unique observation as the zinc oxide absorption was almost not traceable in all other samples. This is a strong indication that the Zn is indeed dissolved in the support and no longer available to form a phase detectable by its characteristic LMCT transition.

The interpretation of the data from the Cu-Fe material family is more difficult due to the overlapping of the copper band and iron band in the UV range (Figure 5.45). The sloping background in the spectra is the consequence of a continuous absorption over the whole spectral range indicative of a collective electron system arising from a multiplicity of compounds. From the literature [Bordiga S., 1996] two common features can be expected for the sample containing Fe; (i) a strong absorption bands in the 300-330 nm interval being due to ligand to metal Fe^{3+} charge transfer character involving isolated framework Fe^{3+} and (ii) broad features in the 330-588 nm related to d-d transition. The d-d transition bands are assigned by considering the Fe^{3+} ion in d^5 configuration in tetrahedral symmetry and this should lead for each specific geometry of iron to five bands at 530 nm, 450 nm, 390 nm and 360 nm [S. Bordiga, 1996]. The broad feature at 751 nm in the spectra of the precursor samples can be interpreted as a d-d transition of Cu^{2+} located in an octahedral environment. The band at 303 and 352 nm represent the overlapping features of d-d transition of Fe^{3+} and LMCT of Cu (II) ions.

Similar observations were made with the data of the weakly reflecting catalytically best Cu-Fe sample B11. There indicate again a high dispersion of the oxide particles allowing to conclude that the active state should also contain highly dispersed Cu metal clusters sitting on iron oxide systems (see also analysis of the BET data). The iron species is interacting with the support giving rise to multiple Fe-O environment such as in poly-oxo-ferrates. After calcination, the iron modified support seems to exhibit some small Cu oxide clusters as indicated from the barely visible copper oxide d-d transition above 800 nm (Figure 5.46). The sample B10 also exhibited poor reflectivity. Contrary to B11, the absence of copper oxide in addition to the sloping background in B10 indicated instead of a uniform highly dispersed cluster morphology the presence of

textural inhomogeneity and surface roughness of the sample. The UV-Vis spectra of calcined sample B09 and B10 shows the appearance a of new absorption band at 837 nm involving d-d transition which only occur with sample Cu-Fe at/at 1:3, and being thus ascribed to the d-d-d transition of Fe^{3+} species.

Table 5.10: UV/Vis band position and their assignments in accordance to literature

Band Position	Assignment
690,751,773,837	d-d transition of Cu(II) in octahedral environment
295, 303, 311	LMCT of isolated Cu (II) ions
300 – 340	LMCT of clustered Cu(II) ions / isolated Fe(III) ions
311	d-d transition of Zn (II) oxide in octahedral environment
347,352	d-d transition of Fe(III) in tetrahedral environment

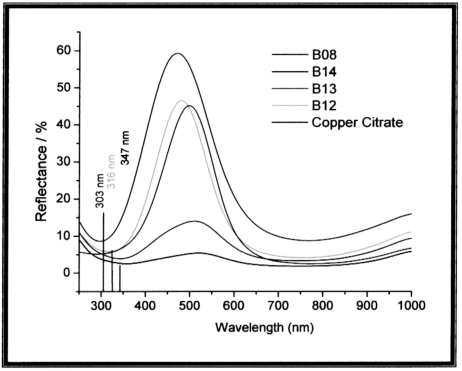

Figure 5.43: DR UV/Vis spectra of precursor Cu-Zn samples supported on SiO_2 prepared via citrate-nitrate route (precursor P2)

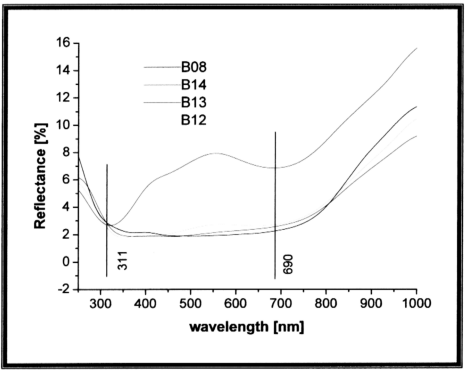

Figure 5.44: DR UV/Vis spectra of calcined Cu-Zn samples supported on SiO_2 prepared via citrate-nitrate route (precursor P2)

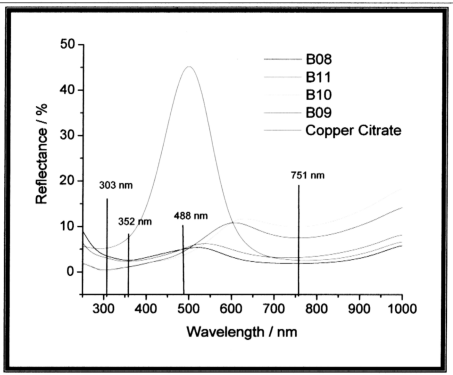

Figure 5.45: DR UV/Vis spectra of Cu-Fe samples supported on SiO_2 prepared via citrate-nitrate route (precursor P2)

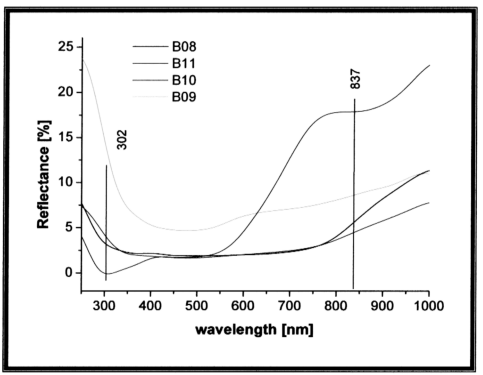

Figure 5.46: DR UV/Vis spectra of calcined Cu-Fe samples supported on SiO_2 prepared via citrate-nitrate route (precursor P2)

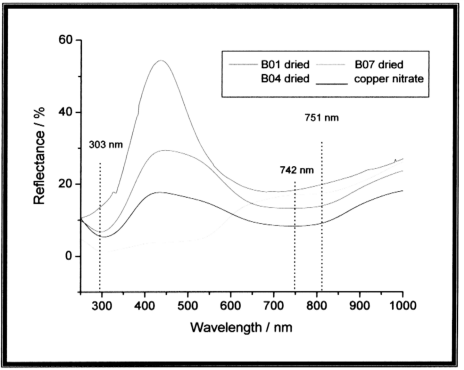

Figure 5.47: DR UV/Vis spectra of precursor samples supported on SiO_2 and prepared via nitrate route (precursor P1)

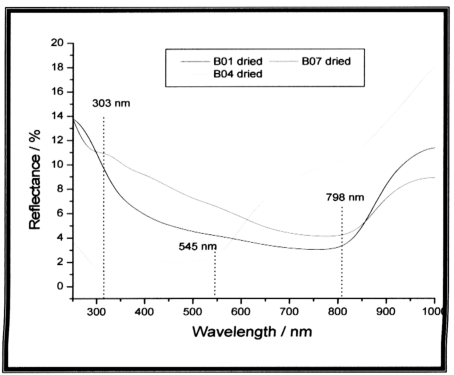

Figure 5.48: DR UV/Vis spectra of calcined samples supported on SiO_2 and prepared via nitrate route (precursor P1)

A key feature of all spectra of the precursor samples of the citrate family is the disagreement of the low energy band edge of the LMCT transition with that measured for pristine Cu citrate. It is clear that besides a possible component at the correct absorption energy the main LMCT transition is blue-shifted for all samples but with a varying extent. The blue shift is interpreted in terms of a more "free" Cu ion *i.e.* of a coordination of Cu not in direct interaction with a strong ligand field as it would be generated by a multi-dentate (4 coordination sites per molecule) citrate ligand. The UV data indicate that the Cu species is at least partly hydrolyzed and the first coordination sphere of the metal ion should contain several weak ligands such as water or hydroxide.

This observation is exactly in parallel to the analysis of the FTIR data for the nitrate complexes. Both spectroscopic techniques indicate thus that the impregnating species were not the expected metal organic complexes but their hydrolysis products. This has severe consequences for the course of the phase formation in the catalyst synthesis: the anchoring of the Cu occurred at low temperatures during drying under hydrothermal synthesis conditions (in wet air) and gave thus rise to the facile incorporation of the active metal species into the support. The extended period of drying applied was only favorable for the loss of a significant amount of the Cu and for the modification of the support oxide.

The calcined samples allowed to conclude in the cases of very poor reflectivity that the intended dispersion of Cu oxides was indeed successful and precluded a sensitive detection of other species present. In those cases where a decent spectrum was obtained it can be concluded from the occurrence of a detectable band edge absorption for the copper species that the copper oxide must be present in such large particles that a collective electronic system with little disruption as common in nano-clusters could be

established. Such samples contain thus large Cu oxide particles and no clusters that are desirable for high catalytic activity.

In summary, UV Vis is a suitable method to study X-ray amorphous samples for the local coordination of both precursors and calcined systems. Although it is speculative to relate catalytic activity that occurs only after a further step of preparation with the spectral properties of the calcined materials, it seems possible to relate the size of the copper oxide systems as detectable by the occurrence of molecular vs. collective excitations to the performance and thus to confirm that small Cu oxide precursors stay small after activation and large Cu oxides do not sufficiently fall apart (as may be expected from a crackling core and shell reduction kinetics) during activation to account for their inappropriate size: the samples exhibit a chemical memory remembering the texture of the precursor in their catalytic performance.

5.1.5. FTIR Characterization

A study of the vibrational spectra by FTIR was carried out on all precursor and calcined samples. The input from this technique will be used to understand the chemical and structural changes of the ligands; before and after sample calcination. The frequency bands, which are of foremost interest in this study will be the fingerprint bands of the metal-citrate complexes. All samples prepared via nitrate route will exhibit the bending vibration of NO_3^- as fingerprint for their complexation.

In the FTIR spectra (Figure 5.49, 5.50 and 5.51), all samples show absorption bands in the region of ~ 1100 cm^{-1} and ~465 cm^{-1} which are assigned to different modes of Si-O-Si or O-Si-O vibrations of amorphous SiO_2 [G.Leofanti *et al.*, 2000], [F.Bocuuzi *et al.*, 1999]. Bands at approximately 1100 cm^{-1} correspond to the stretching vibrations of Si-O bonds; a small shoulder at approximately 970 cm^{-1} is due to the presence of non-bonded oxygen Si-O˙. The bands at ~465 cm^{-1} are attributed to bending vibrations of Si-O and –O-Si-O- bonds, respectively. Unfortunately, two additional peaks were also observed near 1630 cm^{-1} and 1385 cm^{-1} (weak) which should not belong to the bare silica support (Appendix F). The first peak could be contributed by molecular water whereas the later probably due by instrument artifact or contamination.

The vibration of CuO bonds that was reported to appear at 575, 500, and 460 cm^{-1} [Z.Wang, *et al*, 2003] [Boccuzzi F., 1999] cannot be observed due to the presence of a broad band at 465 cm^{-1} from the silica support. In addition, metal bonding is weak in IR due to its selection rules and should be studied by the Raman technique that could not be applied here with the frequency of excitation available in the laboratory.

After loading and drying the support contained significant amounts of precursor complexes as evidenced by the weaker adsorption peak of silica support in the 1100cm^{-1} region for all precursor samples. Broad absorption bands at 3430 cm^{-1} and 1630 cm^{-1} can be assigned to the stretching vibrations of OH species and molecular H_2O, respectively [G. Leofanti *et al.*, 2000]. On the other hand, the band at 3124 cm^{-1} which can be observed only in precursor samples prepared via the citrate-nitrate route arises from the stretching C-H vibration of the citrate ligand. This band is neither observed in other calcined nor nitrate samples.

The acid ligand (citric acid) and its complexes exhibits two strongly coupled C-O bonds with bond strengths intermediate between C=O and C-O. The carboxylate ion gives rise to two bands; a strong asymmetrical OCO stretching band near 1630 cm^{-1} and a weaker symmetrical OCO stretching band near 1300-1400 cm^{-1}. This absorption interferes with a signal at 1385 cm^{-1} arising from the the bending vibration of NO_3^- (Table 5.11 and 5.12). Would nitrate be coordinated to a transition metal then we would have to observe two bands in the frequency range of 1700- 1800 cm^{-1} and 1250-1310 cm^{-1}. The fact that the two strong absorption bands for nitrate coordinated to metal are absent in all spectra indicates clearly that the metal ions are not present as monodentate or chelating nitrato-complexes but rather as aquo complexes with nitrate in the outer coordination shell as non-coordinated counter ion. [M.R. Rosenthal, 1973]

The FT-IR spectra of calcined samples are shown again on top of the precursor samples in Figure 5.49, 5.50 and 5.51. It is observed that after heat treatment at 723 K, the peak at 1385 cm^{-1} correlated to NO_3^- and asymmetrical OCO stretching band was apparently not totally eliminated. The feature seen in the spectra is most likely due to an artifact of the spectrometer and no real absorption and as can be concluded from the highly

uncharacteristic line profile of this signal. The appearance of this artifact indicates that the optical density of the wafers were very high and the IR light transmitted was at the detection limit of the instrument. Caution should thus be taken in interpreting this as residual nitrate ligands as the peak is also observed in the bare silica. Nevertheless, the clear decrease of the characteristic bands of carboxyl group, the disappearance of the C-H bands the strong alteration of the NO_3^- fingerprint in the IR spectra reveals that the citrate groups and NO_3^- ions have taken part in some reactions during thermal treatment. This is expected as all nitrate and most residue of the organic ligand should have been gasified in the calcination process carried out in air.

In summary, the vibrational analysis that was difficult to perform due to the high optical density of the catalysts has revealed that the calcination procedure has removed all discernible traces of molecular organic ligands and also all nitrate. More importantly, it could be shown that the metal ions are not coordinated by nitrate but by water (or hydroxo) ligands and that the nitrate is only present as non-coordinating counter ion. This explains clearly the propensity of the metal species to dissolve in the support oxide as they are hydrolyzed at very low temperature presumably already during drying in air and find then direct contact to the hydroxylated surface of the support. The intended protection of the metal complexes from atomic interaction with the support did not take place as the synthesis conditions did not allow the expected coordination compounds to be present under the reaction conditions chosen.

Table 5.11: FT-IR adsorption band position and their assignments for samples prepared via citrate-nitrate route (precursor P2).

Band (cm^{-1})	Observation and Band Assignment	
	Precursor Samples	**Calcined Samples**
3430	Stretching vibration of OH species	Stretching vibration of OH species
3124, 3180	C-H vibration of ligand	Disappeared after calcination
≈1630	OCO asymetrical stretching of ligand (citric acid). Also molecular water.	Very weak band observed. OCO asymetrical stretching of ligand (citric acid). Also molecular water.
1385	Bending vibration of NO_3^- and OCO symmetrical stretching band of citric acid.	Weaker band observed compared to precursor samples. The sharp line observed in this line could also be artifacts.
1100	-Si-O stretching vibration of silica (weak in samples as compared in bare silica)	Si-O stretching vibration of silica
465	-O-Si-O vibration of silica (weak in samples as compared in bare silica)	-O-Si-O vibration of silica.

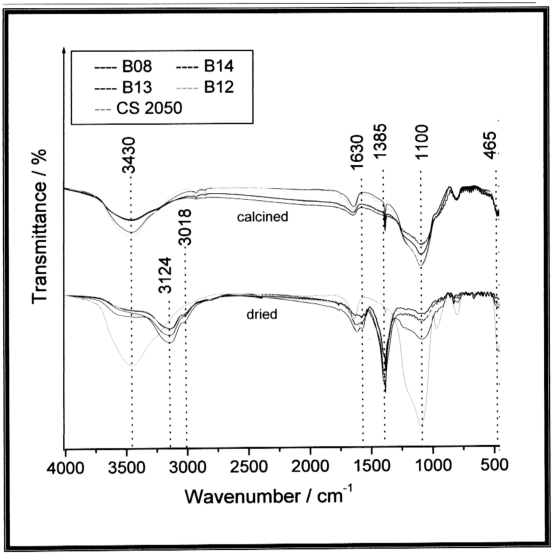

Figure 5.49: FTIR spectra of precursor and calcined Cu-Zn samples supported on silica; prepared via citrate-nitrate route (precursor P2).

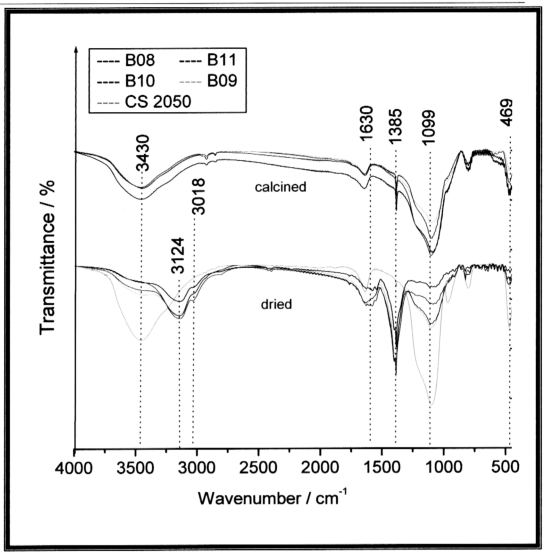

Figure 5.50: FTIR spectra of precursor and calcined Cu-Fe samples supported on silica; prepared via citrate-nitrate route (precursor P2).

Table 5.12: FT-IR adsorption band position and their assignments for samples prepared via nitrate route (precursor P1).

Band (cm^{-1})	Observation and Band Assignment	
	Precursor Samples	**Calcined Samples**
3430	Vibration of OH species	Vibration of OH species
≈1630	Molecular water.	Molecular water.
1385	Bending vibration of NO_3^-	Weaker band observed compared to precursor samples. The sharp line observed in this line could also be artifacts.
1100	-Si-O stretching vibration of silica (weak in samples as compared in bare silica)	Si-O stretching vibration of silica
465	-O-Si-O vibration of silica (very weak in samples)	-O-Si-O vibration of silica.

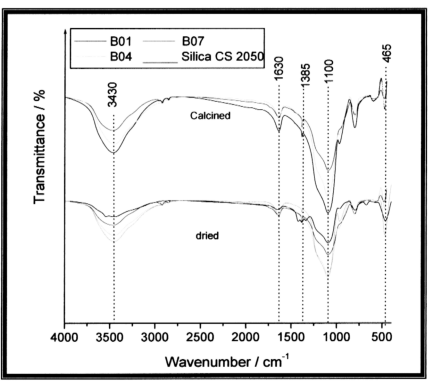

Figure 5.51: FTIR spectra of precursor and calcined samples supported on silica; prepared via nitrate route (precursor P1).

5.2 Thermal Analysis

5.2.1. TGA, DTG and DSC

The calcination procedure adopted during the screening campaign was chosen based on the best calcination temperature adapted from the high throughput optimisation work done on the hydrogenolysis of methyl acetate. All 28 catalysts in this work have observed this procedure strictly in air atmosphere.

A key objective in the preparation of active and selective hydrogenation catalysts is to achieve nano-scale copper from copper oxide (supported or otherwise). One of the most relevant preparation steps in this objective is the calcination procedure. The lowest possible temperatures to achieve complete conversion of the precursors into oxides are required and a complete gasification of all volatile ligands is essential for undisturbed interactions of the active oxide with the support. In view of this, a series of sample precursors was measured using the TGA and DSC method; to obtain meaningful information of the nature of precursor presence and the decomposition processes. The TGA temperature program chosen was a linear ramp from 300 – 900 K at a heating rate of 5 K min^{-1}; synthetic air flow rate of 50 mL/min whereas DSC was performed complementary to the TGA techniques. Due to the common technical limitation of DSC here only an autogeneous atmosphere diluted with nitrogen could be used. Measurement results were grouped by catalyst series (Cu-Zn or Cu-Fe prepared via P1 and P2) and depicted as in Figure 5.52 to Figure 5.61.

Comparative analysis of the results indicates that the same mechanism of ligand decomposition is involved in all nitrate cases (B01, B04 and B07). It is obvious that the same processes were registered as by the TGA and DSC curves (Figure 5.52, 5.54, 5.60

and 5.61). The enthalpies of the processes were determined based on the DSC measurements and are presented in Table 5.13 to 5.14. The two and three endothermic processes in B01, B04 and B07 respectively, which were accompanied by mass loss, could correspond to the complex dehydration and thermal decomposition of the nitrates. As a result, stable oxides are formed at the end of complete decomposition.

According to Z. Ding [Ding Z., 2002], during the thermal decomposition of copper nitrate, a high surface energy material is produced which causes the reduction of nitrogen dioxide to nitric oxide. Z. Ding further suggested that the copper nitrate dissolves in its own water of crystallization; the copper nitrate then hydrolyzes to copper oxy-nitrate and nitric acid. This nitric acid then decomposes on the copper oxide surface to nitric oxide and nitrogen dioxide. The following reactions are postulated:

$$Cu(NO_3)_2 . 3H_2O \longrightarrow CuOH. NO_3 + HNO_3 + 2\ H_2O$$
$$2\ HNO_3 \longrightarrow H_2O + 2\ NO_2$$
$$NO_2(CuO) \longrightarrow NO + \tfrac{1}{2}\ O_2 + CuO$$

However, based on the characteristic pattern of material in the studies, the first and second process in the temperature range of 300-700 K as exhibited in the TGA measurement in samples should be associated to the melting of the compound and partial dehydration given as:-

$$M(NO_3)_2.nH_2O \longrightarrow M(NO_3)_2.3H_2O + (n-3)H_2O$$
$$2M(NO_3)_2.3H_2O \longrightarrow M_2(NO_3)_2(OH)_2 + 3H_2O + 2NO_2$$

The proposed resulting material after the second process above would be a metal nitrate hydroxide which is in agreement with XRD. The third and fourth processes which occur

in the temperature range of 700-900 K comprise the formation of the anhydrous nitrate that is metastable against loss of nitric oxide. The condensation step of initially formed hemi-nitrates to an oxonitrate and free oxygen (autoreduction of ligand) is followed by a final decomposition into the oxide and a final nitrate ligand.

$$M_2(NO_3)_2(OH)_2 \rightarrow MO.MONO_3 + H_2O + NO_2$$
$$MO.MONO_3 \rightarrow M_2ONO_3 + 1/2O_2$$
$$M_2ONO_3 \rightarrow 2MO + NO_2$$

where M representing binary catalyst system, comprises of supported Cu-Zn or Cu-Fe

This scenario from literature studies is, however not in agreement with the stoichiometries that are deduced from the weight losses as recorded in Tables 5.13. The expected weight loss of a metal nitrate being converted into an oxide would be about 56% using the average molecular weights of Cu and Zn respectively. Even with the very optimistic assumption that no water would be present in the compound after the first endothermic loss it occurs that the weight losses observed do not:

- account for the metal loading; much of the metal must be present already without nitrate ligands
- fall in line with the multi-step process outlined above.

The experiments rather indicate that after partly dehydration at about 400 K a combined reaction of ligand removal and polycondensation did occur. The data are summarized in Table 5.15. It is clear that a major part of the metal loading has lost their nitrate ligands upon precipitation/anchoring. This analysis agrees well with the conclusions from the spectroscopic studies indicating a major presence of aquo-complexes. The analysis is further well supported by the DSC curves shown in Figure 5.60. The two traces from the nitrate samples exhibit two well-separated endothermic events for dehydration and

for polycondensation. The condensation process is a multi-step reaction occurring maybe according to the sequence suggested in the literature. It is significant that the kinetics of the oxide formation is different in the two samples shown as can be seen from the differences in line profiles. The differences in peak temperature of the main event indicates that kinetic hindrance may have played a role as the more abundant nitrate (B07) exhibits the higher peak temperature. It can be expected that large crystals with substantial transport hindrances for evolving gasses will be formed from these precursors. The narrow line profile indicates a fast overall reaction expecting whisker-like aggregates of oxide rather than finely divided small particles. The data also fit well with the observation of crystalline tenorite in the XRD analysis.

The decomposition of precursor P2, metal citrate-nitrate is more complicated and is also known as the auto-combustion technique. This technique involve the usage of citric acid, which has three carboxylic and one hydroxyl group for coordinating to metal ions, and therefore prevents the precipitation or phase separation and provides an intimate blending among the constituents ions. It is a low cost material and can be combusted with nitrates at a low ignition temperature (475-575K) and therefore provides a good choice of fuel in the combustion technique. The pH 7 for all citrate-nitrate solutions also was chosen to prevent any possibility of phase separation during the gel formation, and in addition, all metal solutions are most stable at room temperature at this pH. Teraoka *et al.* showed that dilute NH_4OH not only helps in dissociation of citric acid to provide more coordination sites for metal ions, but it also improves the solubility of the metal nitrates [Purohit R.D, 2002].

When the precursor solution (mixed solution of the metal nitrate and citric acid) is heated at around 353-373 K (the region of 1st weight loss from TGA analysis),

dehydration takes place followed by gelation. The gelation probably results due to the formation of a metal-citrate-nitrate complex which is formed from the complex mixture of metal citrate complexes, coordinated nitrate anions and ammonium from reagents used to adjust the pH of the precipitation solution. According to literature, this mixture will undergo auto-iginition process (exothermic) under limited oxygen condition. With assumption that no elemental carbon from polycondensation of the complex ligand will form, the following approximate reaction was postulated:-

(A) $M(C_6H_6O_7)_8.(n+6)H_2O \rightarrow M(C_6H_6O_7)_8.6H_2O + nH_2O$
(B) $M(C_6H_6O_7)_8.6H_2O \rightarrow M(C_6H_6O_7)_8 + 6H_2O$
(C) $M(C_6H_6O_7)_8 \rightarrow M(C_5H_6O_6)_8 + 8CO$
(D) $M(C_5H_6O_6)_8 \rightarrow M(CO_2)_3 + 8(CH_3COCH_3) + 13CO_2$
(E) $M(CO_2)_3 \rightarrow MO + 3CO_2$

where M representing binary catalyst system, comprises of supported Cu-Zn or Cu-Fe

The fact that higher percentages of carbon were observed in some of the inactive samples from SEM images was not a good indicator, as the elemental carbon as coke must have formed under autogenic reaction condition previously mentioned. Every effort should be taken to avoid the deposit of coke on the silica as together with the metal oxide it will result in severe de-activation of the metal during activation under hydrogen and/or encapsulation of the metal particles. Therefore, great care should be taken in future preparation to control the chemical potential of the calcination atmosphere.

Unfortunately, the quantification of the TGA data together with their qualitative interpretation augmented by the DSC data prove that the notion about structure and function of the citrate-nitrate is not correct and in addition, that significant differences exist between the chemical composition of Cu-Zn and Cu-Fe samples.

The DSC data show clearly that the first weight loss step is the loss of water as an endothermic event is registered in DSC. The sharp main weight change is due to the extremely fast exothermic event seen as spike in the DSC traces. This feature indeed justifies the notion about auto-ignition of the ligand internal reaction between citrate and nitrate. The weaker final weight loss is accompanied by a strongly exothermic signal (normalized to the amount of material lost) indicating that a highly exothermic total combustion reaction accounts for the signal. This is in line with the formation and partial combustion of soot from the explosive decomposition of the citric acid. There is no indication of the careful polycondensation of citric acid in more carbon-rich oligomers prior to ignition that was described in literature studies.

Taking into account the small weight change of the soot gasification it is now possible to assign the second weight change to the process of ligand removal and the first weight loss to the dehydration of the metal-citrate complexes. If this assignment is correct one can work out from the stoichiometry changes the average coordination of the metals and the extent to which the non-Cu metal was indeed atomically disperse integrated into the precursor complex as expected from the application of the fourfold coordinating ligand citric acid. The content in metals is given in Table 5.15 as wt% oxidic form in order to be consistent with micro-analytical EDX data discussed in section 5.1.3. Inspection of the data in Table 5.15 allows for the following conclusions:

- The citrate method starts from metal-citrate 1:1 complexes. The medium-strong citric acid is not fully deprotonated at pH 7 and can thus function as two-base anion for a copper hexa-aquo complex.
- The weight losses for Cu-Zn agree exactly with the expected values for the Cu-only loading indicating that no homogeneous intermetallic Cu-Zn precursor was formed but rather a copper-citrate and a Zn nitrate outer orbital complex.

- In the Cu-Fe system, however, the weight losses agree well with a mixed Fe-Cu citrate compound using nitrate and OH^- as counter ions. This significant difference accounts well for the textural differences found in the BET analysis pointing to a polymeric support iron oxide carrying the Cu oxide particles.
- The exception B13 of a very Zn rich composition shows that a small amount of Zn is incorporated in the Cu-water complex which in turn has absolutely no positive effect on catalysts as the activity per copper loading is exactly identical for B13 and B14 the best-of-all system. There is no bimetallic catalytic effect but the second metal has the function of a structural promoter of the fixation of the Cu.
- The very iron rich sample B10 seems to exhibit the theoretical content of Fe and Cu species in contrast to the EDX analysis. It can be expected that large agglomerates of iron oxides precluded a meaningful averaging of the point EDX data and thus gave rise to incorrect values of composition.

The DTG curves in Figure 5.53 and 5.55 bring about a detail of the kinetics of the citrate decomposition. Only the Cu-rich samples B08 and B14 exhibit a clean and complete reaction within the time-temperature window of the main step. The diluted samples B12 and B13 indicate that a delayed process of presumably carbon combustion follows the instant decomposition step.

This observation points to the fact that Cu is also active catalytically in the ligand decomposition process as activated Cu-oxide just being formed. It is interesting to see that the catalyst catalyzes its own formation by supporting the gasification of its precursor. The observation leads to the recommendation to consider small additives of strongly oxidizing promoters to the formulation of the catalysts in order to further

reduce the end calcination temperature and to enhance the dispersing effect of an explosion-like ligand decomposition.

In summary, the TGA-DTG and DSC data gave a consistent picture of the thermal reactivity of the samples allowing to conclude several points for further catalyst development. It is obvious that the experimental "optimum" calcination temperature of 723 K is far too high and should be reduced by 200 K minimum. It can be expected that inappropriate reactor conditions during calcinations led to kinetic hindrance of gas transport and thus created an erroneously high end temperature for complete ligand removal. Slow heating, a dwell time and a controlled gas exchange must be ensured in calcination of such highly loaded systems that can barely be designated as "impregnated".

The choice of pH 7 for the impregnation solution of the citrate is probably sub-optimal as it supports partial protonation of the citrate and thus hydrolysis of the metal complexes with the fact that at least inhomogeniety in the inner-outer orbital composition of the metal complexes exist. This fact is well supported by the visual observation that fresh precursors appear in a variety of shades of blue that indicate the coordination isomer between weakly aquo ligands (light) and strongly binding citrate ligands (dark).

The abundance of the modifier metal M2 should be made much lower than in the present formulations as the intended alloying in the final catalyst designated as "bimetallic" is definitively not realized and M2 just blocks sites for deposition of Cu clusters. This conclusion is well supported by the trends in catalyst performance reported earlier in this work and summarized in Table 5.1.

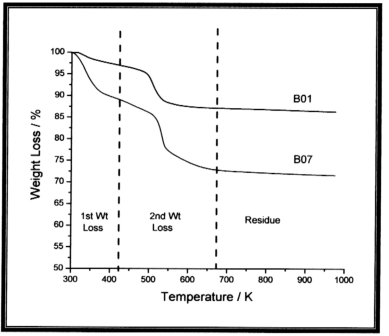

Figure 5.52: Thermal Gravimetry Analysis of B01 and B07, sample precursors prepared via nitrate route, precursor P1.

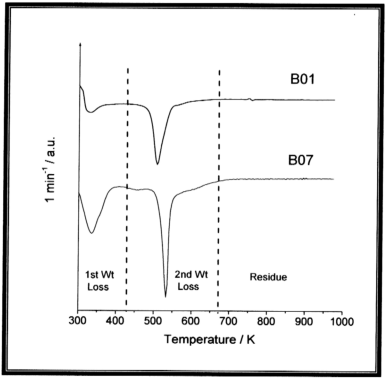

Figure 5.53: Differential Thermal Analysis (DTG) of B01 and B07, sample precursors prepared via nitrate route, precursor P1.

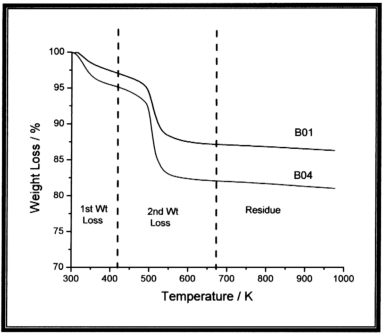

Figure 5.54: Thermal Gravimetry Analysis of B01 and B04, sample precursors prepared via nitrate route, precursor P1.

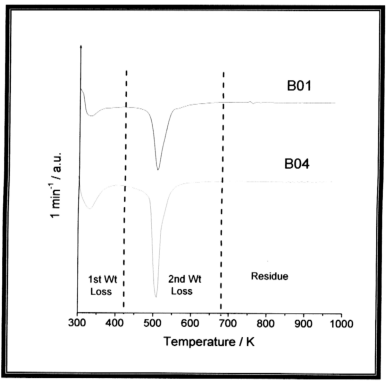

Figure 5.55: Differential Thermal Analysis (DTG) of B01 and B04, sample precursors prepared via nitrate route, precursor P1.

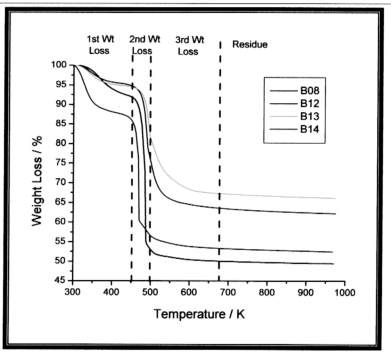

Figure 5.56: Thermal Gravimetry Analysis of Cu-Zn sample precursors (including mono-copper sample) prepared via nitrate-citrate route, precursor P2.

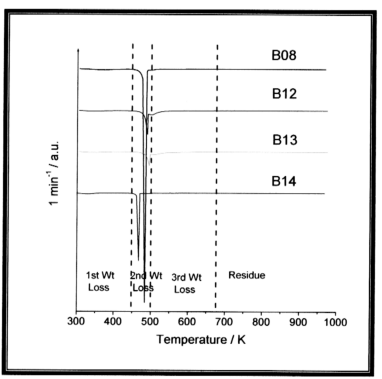

Figure 5.57: Differential Thermal Analysis (DTG) of Cu-Zn sample precursors (including mono-copper sample) prepared via nitrate-citrate route, precursor P2.

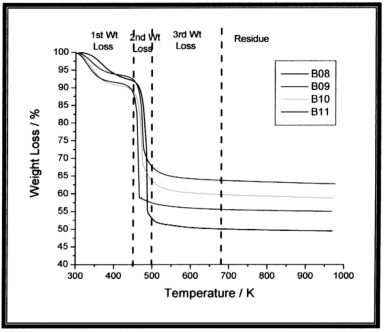

Figure 5.58: Thermal Gravimetry Analysis of Cu-Fe sample precursors (including mono-copper sample) prepared via nitrate-citrate route, precursor P2.

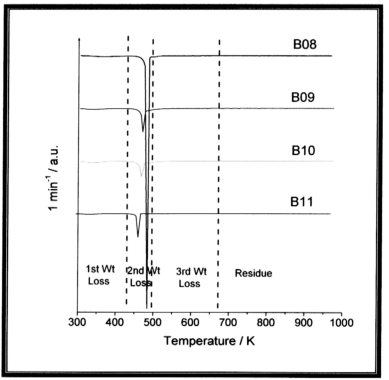

Figure 5.59: Differential Thermal Analysis (DTG) of Cu-Fe sample precursors (including mono-copper sample) prepared via nitrate-citrate route, precursor P2.

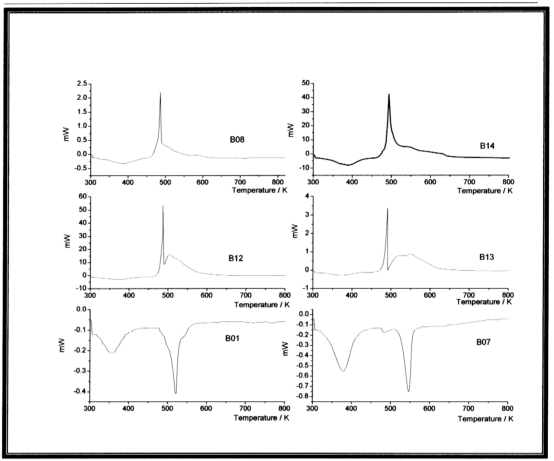

Figure 5.60: DSC thermogram of Cu-Zn precursor samples (including mono-copper samples) prepared via precursor P1 and P2.

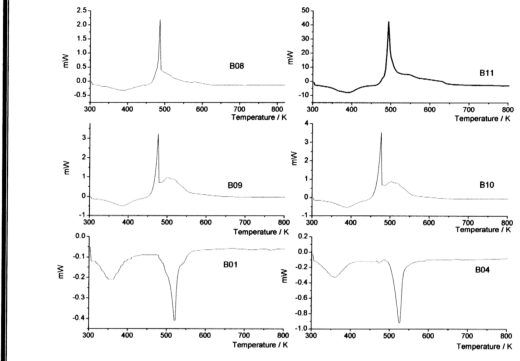

Figure 5.61: DSC thermogram of Cu-Fe precursor samples (including mono-copper samples) prepared via precursor P1 and P2.

Table 5.13: Weight Loss at various steps and temperature as obtained from the thermal analysis data.
(highlighted in yellow for precursors prepared via P1, blue for Cu-Zn series prepared via P2, green for Cu-Fe series prepared via P2 and none for mono-copper copper prepared via P2).

Catalyst Code	1st Weight Loss		2nd Weight Loss		3rd Weight Loss		4th Weight Loss		Residue
	T_R and T_{TG}	Wt Loss (%)	T_R and T_{TG}	Wt Loss (%)	T_R and T_{TG}	Wt Loss (%)	T_R and T_{TG}	Wt Loss (%)	
B01	T_R: 303-401 T_{min}: 329	2.4722	T_R: 401-703 T_{min}: 507	10.2710	T_R: 703-973 T_{min}: 827	0.8273	-	-	86.2532
B07	T_R: 303-391 T_{min}: 340	10.3357	T_R: 391-489 T_{min}: 436	3.1670	T_R: 489-786 T_{min}: 534	14.3350	T_R: 786-973 T_{min}: 880	0.5667	71.5687
B04	T_R: 303-397 T_{min}: 330	4.7821	T_R: 397-693 T_{min}: 509	13.2720	T_R: 693-973 T_{min}: 803	0.9077	-	-	86.2532
B08	T_R: 303-433 T_{max}: 353	8.0050	T_R: 433-548 T_{max}: 474	41.1928	T_R: 548-973 T_{max}: 761	1.2861	-	-	49.5121
B12	T_R: 303-415 T_{max}: 349	4.5204	T_R: 415-492 T_{max}: 489	16.6635	T_R: 492-728 T_{max}: 504	15.6360	T_R: 728-973 T_{max}: 850.61	0.9710	62.2298
B13	T_R: 303-430 T_{max}: 338	5.0802	T_R: 430-499 T_{max}: 495	13.7777	T_R: 499-768 T_{max}: 513	14.0152	T_R: 768-973 T_{max}: 871	0.9810	66.1443
B14	T_R: 303-450 T_{max}: 355	12.6883	T_R: 450-547 T_{max}: 473	27.7760	T_R: 547-973 T_{max}: 760	1.0847	-	-	52.4875
B09	T_R: 303-410 T_{max}: 344	6.2944	T_R: 410-683 T_{max}: 471	30.0718	T_R: 683-973 T_{max}: 828	0.9247	-	-	54.9967
B10	T_R: 303-419 T_{max}: 343	9.1328	T_R: 419-673 T_{max}: 465	31.0956	T_R: 673-973 T_{max}: 823	0.9881	-	-	62.7244
B11	T_R: 303-435 T_{max}: 352	8.9891	T_R: 435-528 T_{max}: 483	32.9389	T_R: 528-973 T_{max}: 751	1.8363	-	-	49.5121

T_R = Temperature range T_{max} = Temperature maximum (exothermic) T_{min} = Temperature minimum (endothermic)

Table 5.14: DSC results of dried precursor samples
(highlighted in yellow for precursors prepared via P1, blue for Cu-Zn series prepared via P2, green for Cu-Fe series prepared via P2 and none for mono-copper copper prepared via P2).

Precursor Samples	DSC					
	1st Transition		2nd Transition		3rd Transition	
	T_R and T_{endo} (K)	ΔH / Jg^{-1}	T_R and $T_{endo/exo}$ (K)	ΔH / Jg^{-1}	T_R and $T_{endo/exo}$ (K)	ΔH / Jg^{-1}
B01	T_R = 303-423 T_{endo} = 357	61.80 Endothermic	T_R = 423-673 T_{endo} = 503	109.48 Endothermic	-	-
B07	T_R = 303-453 T_{endo} = 378	251.85 Endothermic	T_R = 303-503 T_{endo} = 483	12.62 Endothermic	T_R = 503-673 T_{endo} = 547	162.27 Endothermic
B04	T_R = 303-423 T_{endo} = 359	133.68 Endothermic	T_R =423-493 T_{endo} = 473	7.28 Endothermic	T_R = 493-673 T_{endo} = 526	221.46 Endothermic
B08	T_R = 303-453 T_{endo} = 387	155.94 Endothermic	T_R = 453-493 T_{exo} = 488	352.25 Exothermic	T_R = 493-673 T_{exo} = 491	290.45 Exothermic
B09	T_R = 303-453 T_{endo} = 385	297.39 Endothermic	T_R = 453-493 T_{exo} = 478	344.81 Exothermic	T_R = 493-673 T_{exo} = 501	811.36 Exothermic
B10	T_R = 303-453 T_{endo} = 390	346.14 Endothermic	T_R = 453-493 T_{exo} = 478	468.52 Exothermic	T_R = 493-673 T_{exo} = 504	644.88 Exothermic
B11	T_R = 303-453 T_{endo} = 384	175.88 Endothermic	T_R = 453-493 T_{exo} = 491	452.51 Exothermic	T_R = 493-673 T_{exo} = 523	516.42 Exothermic
B12	T_R = 303-453 T_{endo} = 374	99.35 Endothermic	T_R = 453-493 T_{exo} = 486	294.98 Exothermic	T_R = 493-673 T_{exo} = 503	988.48 Exothermic
B13	T_R = 303-453 T_{endo} = 375	108.27 Endothermic	T_R = 453-493 T_{exo} = 491	240.47 Exothermic	T_R = 493-673 T_{exo} = 533	903.11 Exothermic
B14	T_R = 303-453 T_{endo} = 389	255.41 Endothermic	T_R = 453-493 T_{exo} = 494	514.65 Exothermic	T_R = 493-673 T_{exo} = 543	550.79 Exothermic

T_R = Temperature range T_{exo} = Temperature maximum (exothermic) T_{endo} = Temperature minimum (endothermic)

Table 5.15: Comparison of the metal oxide content by EDX and by TGA

Samples	Method	Weight % of Cu		Total Weight % of Metal		Comparative Weight % of Metal by TGA
		cal.	exp.[a]	cal.	exp.[b]	exp.[c]
B01	nitrate	41.02	40.88	41.02	40.88	6.2
B07	nitrate	29.56	28.14	39.68	38.28	9.8
B04	nitrate	25.36	25.15	32.82	32.10	8.0
B08	citrate-nitrate	28.81	28.06	28.81	28.06	28.8
B12	citrate-nitrate	14.06	14.59	28.49	26.67	14.5
B13	citrate-nitrate	6.95	5.38	28.35	26.01	9.6
B14	citrate-nitrate	21.35	20.65	28.65	27.19	19.5
B09	citrate-nitrate	11.79	10.76	22.19	20.71	21.0
B10	citrate-nitrate	5.46	5.45	19.93	11.37	21.0
B11	citrate-nitrate	19.11	18.16	24.85	22.59	23.1

cal. = calculated value

exp. = experimental value obtained from analytical measurement(s).

[a,b] experimental value derived from EDX measurements on samples (refer to page 125).

[c] experimental value derived from TGA measurements on samples.

5.2.2. Reduction Behavior

Thermoanalytical techniques are widely used methods for the characterization of the properties and reactivity of solid materials [Ertl G., 1997c]. As a finely divided metallic copper has been identified to be the catalytically active component, it is appropriate to use TPR for investigating the kinetics of the generation of the active Cu species. Its quantification can give information about the availability of the Cu for reduction into active species.

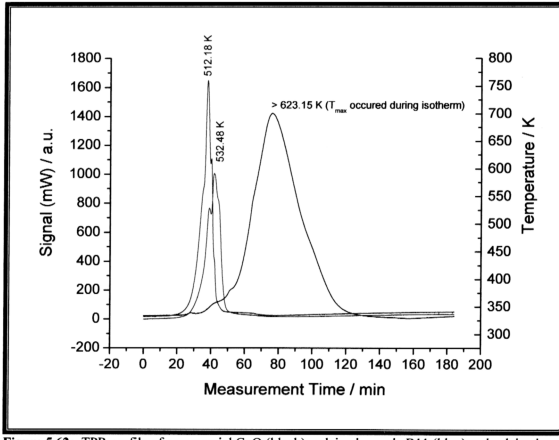

Figure 5.62: TPR profile of commercial CuO (black), calcined sample B11 (blue) and calcined sample B14 (red), parameters mimicking the reduction procedure at 623 K, 5 K min^{-1} and isotherm for 2 hours.

Figure 5.62 reports the TPR profile of commercial CuO obtained from Aldrich, purity 99% with particle size < 5 micron as reference and of the best calcined materials from each of the catalyst series *i.e.*, B14 and B11. The gas composition of 5% hydrogen

(balance nitrogen) was adjusted to mimic the chosen reduction conditions carried out in the high throughput activation (pre-treatment) unit as described in chapter 3. The CuO sample was reduced incompletely under the chosen temperature conditions to minimize the reduction signal and to allow the resolution of the pre-peaks at about 100 K lower than the main reduction occurring at about 640 K. These pre-peaks are relevant as they indicate the lowering in reaction temperature gained from the defects present in the polycrystalline material. It is seen that this gain in activity is well comparable to the position of the reduction events for the well-performing catalysts allowing one to conclude that:

- Such a lowered reduction temperature is by no means a sign of mixed oxide or alloy formation as often speculated in the literature (see below)
- The nature of the CuO species on the catalysts is hardly affected by the second metal M2 (except the small relative shift of the two line groups)
- The structure of the CuO prepared by calcination should be similar to the defective material present in genuine and crystalline CuO which is in full agreement with the XRD results
- The resolution of the expected two step process of CuO reduction to Cu_2O as intermediate and then to Cu metal (two lines in 1:1 intensity ratio) cannot be achieved with this method (if the origin of the peak splitting were this intermediate formation it should be the same for the two catalyst systems)
- The fine structure of the reduction peak being indicative of various reduction kinetics for different types of particles of *e.g.* different shape or size or different content of defects. The TPR profile is thus a sign for the polydispersity of the CuO precursor particles. It can be expected that a wider spread resulting in a wider separation of the features in TPR should be an indication for a poorer

catalyst if one assumes that monodisperse small and highly reactive (defective) particles are best for high performance systems.

According to the literature for copper and zinc containing methanol synthesis catalysts, the evidence of extensive dissolution of a positively charged copper species in the zinc oxide lattice was speculated when the catalyst had been reduced at 523 K [Metha S. *et al.*, 1979]. Therefore, the multiple reduction peak of B14 at 450-550 K (Figure 5.58) would originate from the reduction of an oxidic copper species in the promixity of zinc oxide or zinc silicate. The copper metal that is formed by reduction of the Cu^{2+} species in mixed oxides should form finely dispersed particles, which form a two-dimensional epitaxial layer on zinc oxide (despite a lattice mismatch of a minimum 9.6% which excludes a direct epitactic relation according to all experience in the growth of ordered multilayer systems), according to a model proposed by Okamoto *et al.* [Okamoto Y. *et al.*, 1983] who studied reduced Cu/ZnO methanol synthesis catalysts by X-ray photoelectron spectroscopy (XPS) and Auger spectroscopy

The reduction profile of a Cu-Fe mixed species (under reductive atmosphere -5% hydrogen at a heating rate of 20 K min^{-1}) were reported to occur in two steps:a) 573-600 K; corresponding to the reduction of $CuO \rightarrow Cu^{o}$ and $Fe_2O_3 \rightarrow Fe_3O_4$ (magnetite). b) > 800 K; corresponding to the subsequent reduction of Fe_3O_4 to metallic iron [Bhukur DB., 2002].

Based on this information, it can be concluded that the synthesized material (B11 and B14) are easier to be reduced than bulk copper oxide and that in both samples copper oxide is indeed the reduced species leaving the M2 oxide component untouched.

To gain more information of the reduction behavior of calcined materials from the temperature-programmed method, TPR analysis was carried out for all calcined samples and the results of Cu-Zn and Cu-Fe series are presented in Figures 5.63 to 5.66.

From the Figures 5.63 and 5.65, more prominent reduction profiles were observed with higher copper content in the samples Cu-Zn (precursor P2): B08 > B14 > B12 > B13; and Cu-Fe (precursor P2): B08 > B11 > B09 > B10. It occurs further that the temperature of maximum reduction rate shifts to a lower temperature for the larger peaks in agreement with the notion that little copper is better dispersed on the support and hence more difficult to reduce despite of its higher surface-to-volume ratio which should facilitate a gas-solid reaction. The structural beneficial effect of the second element M2 (Zn or Fe) is also obvious as the best catalyst is not the one with the most available copper and the lowest reduction temperature (B8). The presence of the support modifier (M2 and some Cu eventually) can be seen by the long tail of reduction extending to 950 K which is present in all spectra despite of the fact that the peak picking software did not recognize the high background in all cases as peak (such as in B13). This uncertainty in the determination of the background will have an effect on the accuracy of the integration. As it is likely that some of the supports reduction occurs also concomitant with the CuO reduction the integration may overestimate the extent of reduction of copper. As some copper will also be non-reducible due to dissolution (see uv-Vis and BET sections) there is a partial compensation of two antagonistic sources of errors.

The lineshapes of the reduction profiles are not the same even within each family of samples. This underlines that the nature of the peak splitting is not an intrinsic intermediate being formed but rather the existence of several species of Cu particles differing in e.g. particle size, defect density or degree of interaction with the support. As

in UV-Vis there was ample evidence for at least two types of oxide (large and less defective with a collective plasmon excitation and small and defective with only a local LMCT transition this finding is not surprising. The close proximity of the reduction rate maxima precludes the notion that one form is at the surface and the other may be located as dissolved Cu species. These forms may rather give rise to the background reduction signal. In the quantification of the Cu species present no peaks were included with maximum reduction rate temperatures above of 600 K.

The estimation of the degree reduction of copper was carried out for the Cu-Zn and Cu-Fe series with the results being reported in Tables 5.16 and 5.17. The total hydrogen consumption suggests a near-complete reduction of the CuO for mono-copper catalyst prepared via citrate-nitrate route, B08 (Table 5.16). Its profile consists of one broad reduction peak whereby the onset temperature is apparent already at 440 K. The peak reaches a maximum at 536 K and reduction is complete at about 579 K. Comparatively, only 81.36% mono-copper catalyst, B01 prepared via nitrate route (precursor P1) was reduced (Table 5.17). This is evidence for the supposed stronger trend to dissolve Cu during the melting and coagulation of the mesophase of the molten nitrate-hydroxide intermediate postulated in SEM-EDX, UV-VIS and BET analysis of the samples.

Table 5.16: Data summarized from TPR profile of Cu-Zn calcined samples (including mono-copper samples).

Sample	Reduction Peak, T_{max} / K	Experimental H_2 Consumption / $\mu mol\ g^{-1}$	Calculated H_2 Consumption / $\mu mol\ g^{-1}$ (to reduce copper oxide)	* Max. reduction of copper (%)
B08	a: 536.29	4353.49	4534.00	96.02
B14	a: 547.1	2974.25	3359.00	88.55
B12	a: 546.23:	1093.01	2212.00	119.62
	b: 568.47	1553.08		
B13	a: 567.91	1121.87	1093.00	102.64
	b: 850.30	175.46		
B07	a: 568.76	2132.73	4652.00	88.77
	b: 588.20	1997.47		
	c: 931.60	540.54		
B01	a: 511.20	129.27	6454.00	81.36
	b: 592.89	5121.99		
Silica CS2050	-	-	-	-
C1	-	-	-	-

* Approximate calculation made based on three assumptions: (i) there are no loss of active metal copper during synthesis, (ii) all copper (precursors) transformed to metal oxide(s) after calcination in oxidation atmosphere.

Bare silica support and Zn oxide which exist in the mono-zinc silica C1 (Figure 5.67) did not exhibited any reducible species. On the other hand, the standard reference C2, mono-iron supported on silica (Figure 5.68) gave a broad and complicated TPR profile in the range of 500-800 K. This profile consists of two series of overlapping sequences of reductions of ferric oxide to ferri-ferrous oxide and delayed reduction to Fe metal. It is conceivable that one species is iron oxide forming a massive compound and the more difficult-to-deduce form could be iron oxide in contact or dissolved with the support oxide. The fact that in sample C2 even at the end of the two reduction events there is still about 25% of the iron oxide non-reducible supports the view that not only

dissolution but actually a ternary oxide formation resulting in non-reducible silicates has taken place and three types of iron-containing oxides are present none of which occur in XRD analysis. The high propensity of iron oxo species to undergo autocondensation preferred with respect to dissolution in any oxide matrix would account for the very obvious difference in reduction behavior of the two forms of M2 additives. It is important to note that in the double metallic species there is apparently no overlap of the reduction processes of copper and iron oxides as it would be expected from the linear superposition of the peak of reduction rate of CuO and of the onset of reduction of the iron oxide. This is substantiated from the very incomplete degrees of reduction in the iron-modified catalysts as indicated from the data in Table 5.17. In agreement with the TPR data it can be concluded that compound formation between iron and Cu species in the complexed stages has given rise to a shift in the onset of reduction of iron oxide due to Cu dissolution which in turn is no longer available for Cu metal particle formation.

The nitrate family (see B1, B4 and B7) in Figures 5.64 and 5.66 exhibit much more difficult-to-reduce CuO particles. This is explained by the size of the oxide crystals exhibiting X-ray diffraction and having been identified as to form large and dense aggregates in SEM/EDX. The result of such compact forms is a strong transport hindrance of either evolving water or more likely for Cu of Cu-ions migrating through thick layers of already reduced material. The pre- and post peaks indicate the presence of a few small particles that maybe responsible most for the residual catalytic activity and of deep bulk-dissolved Cu forming silicates rather than being only submerged into the support oxide.

Table 5.17: Data summarized from TPR profile of Cu-Fe calcined samples (including mono-copper samples).

Sample	Reduction Peak, T_{max} / K	Experimental H_2 Consumption / $\mu mol\ g^{-1}$	Calculated H_2 Consumption / $\mu mol\ g^{-1}$	* Max. reduction of metals (%)
B08	a: 536.29	4353.49	4534.00	96.02
B11	a: 525.9	3475.83	5053.00	68.79
	b: 752.41	618.38		
B09	a: 502.93	2323.05	5565.00	41.74
	b: 634.15	333.33		
	c: 830.05	808.24		
	d: 1019.11	1023.20		
B10	a: 498.84	2264.13	6020.00	37.61
	b: 870.95	505.48		
	c: 1006.08	1054.69		
B04	a: 478.83	356.98	6653.00	58.29
	b: 545.08	3521.18		
	c: 785.92	1180.09		
B01	a: 511.20	129.27	6454.00	81.36
	b: 592.89	5121.99		
Silica CS2050	-	-	-	-
C2	a: 654.92	977.06	2321.00	74.21
	b: 765.74	745.38		

* Approximate calculation made based on three assumptions: (i) there are no loss of active metals during synthesis, (ii) all metal (precursors) transformed to metal oxide(s) after calcination in oxidation atmosphere.

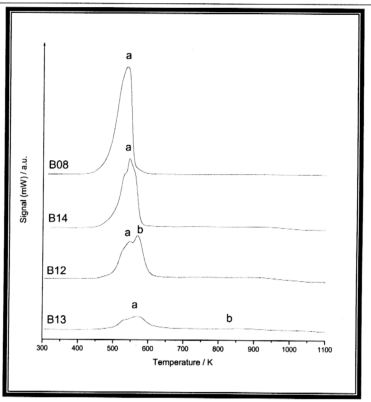

Figure 5.63: TPR profile of calcined Cu-Zn samples (including mono-copper sample) prepared via citrate-nitrate route, precursor P2.

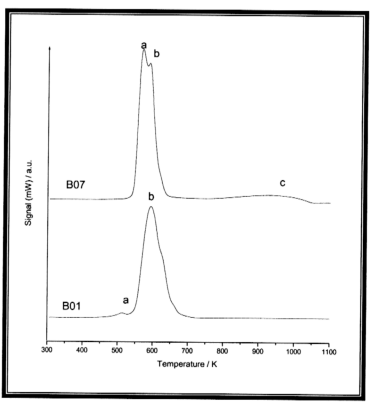

Figure 5.64: TPR profile of calcined Cu-Fe samples B07 and mono-copper sample B01 via nitrate route (precursor P1).

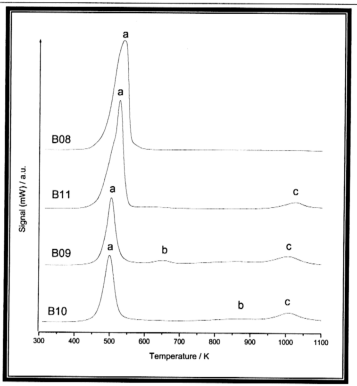

Figure 5.65: TPR profile of calcined Cu-Fe samples (including mono-copper sample) prepared via citrate-nitrate route, precursor P2.

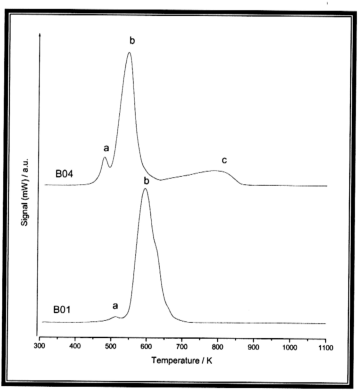

Figure 5.66: TPR profile of calcined Cu-Fe samples B04 and mono-copper sample B01 prepared via nitrate route, precursor P1.

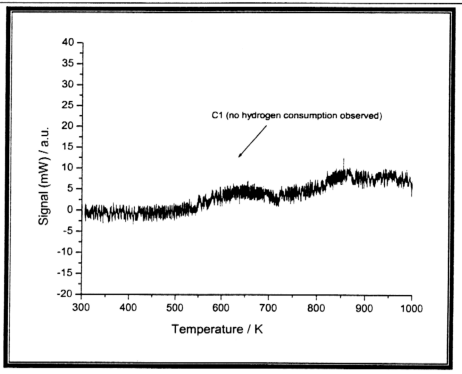

Figure 5.67: TPR profile of standard reference, C1, zinc supported on silica.

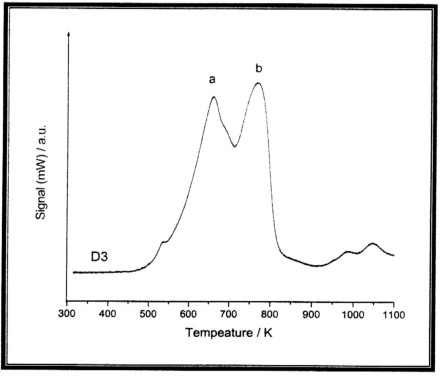

Figure 5.68: TPR profile of standard reference, C2, iron supported on silica.

In summary, TPR has given additional support for the structural description of the catalysts as being Cu particles supported on modified silica. The second element M2 is only responsible of fixing an appropriate form of defective Cu onto the support which is specifically more active that monometallic Cu. The data have given evidence for the presence of a distribution of CuO particles with different reactivity in reduction. As a speculation the present data would suggest that other modifiers M2 that may hold CuO more strongly may lead to even better catalysts. Suggestions would be the non-reducible forms of ceria and zirconia which would increase the peak temperature of reduction but which would hold the resulting Cu particles very strongly through their oxygen-donating interfaces.